water

MDPI

Review

Application of Metal–Organic Framework-Based Composite Materials for Photodegradation of Dye Pollutants in Wastewater

Farzaneh Mahmoudi * and Leonidas G. Bachas *

Department of Chemistry, University of Miami, Coral Gables, FL 33146, USA
* Correspondence: fxm676@miami.edu (F.M.); bachas@miami.edu (L.G.B.)

Abstract: Water pollution is one of the main challenges that severely affects human health and aquatic ecosystems. Chemical pollutants, including industrial waste, agricultural runoff, and clinical sources, can contaminate water. Photocatalytic processes present clean, renewable, and efficient techniques for degrading organic contaminants in wastewater. Metal–organic frameworks (MOFs) are one of the more efficient materials in wastewater remediation due to their significantly high surface area and tunable structures. This review summarizes the development of novel composite materials based on MOFs for the photocatalytic decomposition of dye contaminants in wastewater. Different synthesis methods of MOFs and composite materials are explored. Several strategies for enhancing the photocatalytic activity of MOFs are discussed. Photocatalytic reaction conditions and suggested mechanisms are summarized, particularly for eliminating dye contaminants using MOF-based composite materials. The designed composite materials demonstrate improved stability and photocatalytic activity. This review provides strategies for designing MOF-based composite materials and improving their efficiency and stability for the photocatalytic elimination of dye pollutants in wastewater. Additionally, the review addresses challenges in advancing MOF-based composite materials.

Keywords: MOFs; composite materials; photocatalyst; dye pollutant; wastewater treatment

Citation: Mahmoudi, F.; Bachas, L.G. Application of Metal–Organic Framework-Based Composite Materials for Photodegradation of Dye Pollutants in Wastewater. *Water* **2024**, *16*, 3051. https://doi.org/10.3390/w16213051

Academic Editor: Alexandre T. Paulino

Received: 14 September 2024
Revised: 18 October 2024
Accepted: 21 October 2024
Published: 24 October 2024

1. Introduction

Because of continuous population growth and industrialization, environmental pollution is one of the main global challenges [1–3]. Contaminants from industries, agricultural, personal care, and clinical sources play a significant role in water pollution [4]. Synthetic dyes are widely used in textile printing, paper coloring, and food additives, as well as in the pharmaceutical and cosmetic industries [5]. Some of these dyes are toxic, carcinogenic, and persistent in the environment, which could affect human health and aquatic ecosystems [6]. Using traditional methods like biological treatment, adsorption, and membrane separation has drawbacks like high costs, low efficiency, and formation of secondary contaminants [5]. Recently, advanced oxidation processes (AOPs) have been employed for wastewater remediation. AOPs are characterized by their strong oxidative capabilities, rapid reaction rates, broad applicability, and reduced production of secondary pollutants. Photocatalytic, sonochemical, electrochemical, Fenton, plasma-based oxidation, and ozonation reactions are the most common AOPs. Among those, the photocatalytic oxidation process can degrade pollutants into less-toxic compounds [1,6]. This technique has some advantages, including its simplicity, use of environmentally catalysts, low cost, and high efficiency. A promising photocatalyst has a broad light-absorption range, high number of active sites, efficient charge separation, tunable bandgap, and strong redox capabilities. The structure of the photocatalysts could also be engineered to boost the reactive oxygen species generation and thus improve the degradation of organic contaminants [5]. Most current photocatalysts, like TiO_2 and ZnO, are activated by UV light, have relatively high electron–hole pair recombination which limit their practical usage [6]. In this regard, researchers have developed

efficient photocatalysts with perovskite metal oxides [5], polyoxometalates [7], carbon quantum dots, carbon nitride [8], MXene [9], bismuth oxybromide [10], and metal–organic frameworks (MOFs) [11] for the degradation of organic pollutants in wastewater.

MOFs are a prominent category of porous materials with exceptional physical and chemical properties [2,12]. MOFs with high surface area get considerable attention in wastewater treatment due to their tunable structure, ease of operation, cost-effectiveness, and regulated functions [13]. In 2007, Garcia et al. highlighted the semiconducting properties and charge separation properties of photoactive MOF-5 [14], which ignited interest in the photocatalytic properties of MOFs [15]. The incorporation of redox-sensitive metals and light-harvesting ligands in the structure of MOFs improves their photocatalytic activity. Furthermore, the ultrahigh surface area of MOFs increases the photocatalyst–pollutant interaction, supplying sufficient sites for charge separation and effective photocatalysis. Additionally, the porous structure of MOFs hosts and stabilizes photocatalytic nanomaterials, supplying high accessibility, and allows further modification. Furthermore, MOF material reduces the agglomeration of photocatalysts, acts as electron transfer units, and reduces electron–hole recombination [16]. Additionally, MOFs have applications in drug delivery [17], gas storage, separation [18], energy storage [19], and catalysis [20]. MOFs have been used as an efficient catalyst in biodiesel [21], oxygen and hydrogen evolution reactions, and degradation of organic pollutants in wastewater [22,23]. However, some pristine MOFs show poor light absorption and poor stability in water, which limits their practical applications. To address these limitations, integration of MOFs with functional materials, including metal nanoparticles, metal oxides [24,25], polymers [26], MXene [27], graphene oxide [28], graphitic carbon nitride [29], and metal chalcogenides [15], was investigated.

Recently, prominent development has been made in the designing of MOF-based composite materials to control confinement of guest molecules within specific spaces of MOFs [15]. By efficiently combining the advantages of MOFs and functional materials, the composite materials exhibit improved photocatalytic activity and higher recyclability in comparison to the pristine MOFs. This review aims to examine the literature on MOF-based composite materials for photocatalytic decomposition of dye contaminants in wastewater. It should be noted that catalytic application of MOFs or their composite materials has been extensively reviewed elsewhere. Most of those reviews focused on synthesis methods of MOFs and their applications in different fields [22,23]. In this review, we have limited the scope to photocatalytic degradation of dye pollutants with MOF-based composite materials. In this review, the recent advances in synthesis, characterization, and the photocatalytic activity of MOF-based composite materials towards dyes are summarized. Based on the current progress made in this research field, challenges and future development opportunities are proposed and discussed.

2. Dye Pollutants

Dyes are classified as ionic and non-ionic based on their surface charge. Furthermore, dyes can be categorized by the structure of their chromophore unit into azo, xanthene, indigoid, thiazine, triphenyl methane, diarylmethane, triarylmethane, etc. [6]. Table 1. summarizes common dyes that have been included in this review.

Table 1. List of dyes included in the present review.

Dye	Abbreviation	Charge	Class
Crystal Violet	CV	Cationic	Triphenylmethane
Methylene Blue	MB	Cationic	Thiazine
Rhodamine B	RhB	Cationic	Rhodamine
Azure B	AB	Cationic	Thiazine
Basic Blue 41	BB41	Cationic	Azo
Basic Red 46	BR46	Cationic	Azo
Methyl Orange	MO	Anionic	Azo

Table 1. *Cont.*

Dye	Abbreviation	Charge	Class
Congo Red	CR	Anionic	Azo
Reactive Black 5	RB5	Anionic	Azo
Acid Black 1	AB 1	Anionic	Azo
Rose Bengal	RB	Anionic	Xanthene

3. Metal–Organic Frameworks (MOFs)

MOFs are a class of crystalline porous materials consisting of metal nodes connected by organic linkers forming diverse architectures. The metal ions form complexes with distinct coordination modes, including tetrahedral, square planar, trigonal bipyramidal, and octahedral geometries [1]. The common metal ions for synthesis of MOF are zinc, iron, titanium, aluminum, copper, and zirconium [11]. MOFs are categorized into groups according to their organic linkers as, for example, isoreticular metal organic frameworks (IRMOFs), materials of Institute Lavoisier (MILs), pocket-channel frameworks (PCNs), University of Oslo (UiOs) frameworks, and zeolitic imidazolate frameworks (ZIFs) [30]. The pH of the reaction mixture, temperature, pressure, reaction time, reactant concentration, and solvent are some parameters that affect the physical and chemical characteristics of MOFs [30,31]. The solvothermal technique is the most common method for preparing MOFs. However other procedures included co-precipitation and slow evaporation, as well as sonochemical, electrochemical, and microwave-assisted processes [30,32]. More details are inserted in Figure 1. Moreover, MOFs can be designed according to specific adsorbate targets to increase the related interactions and improve the adsorption performance [30]. The stability and reusability of MOFs are crucial factors that should be considered in the development of photocatalysts for wastewater remediation. Some MOFs demonstrate low stability, which is affected by parameters like humidity, pH of solution, and temperature. Addressing these issues is essential to optimizing the photocatalytic activity of MOFs [30].

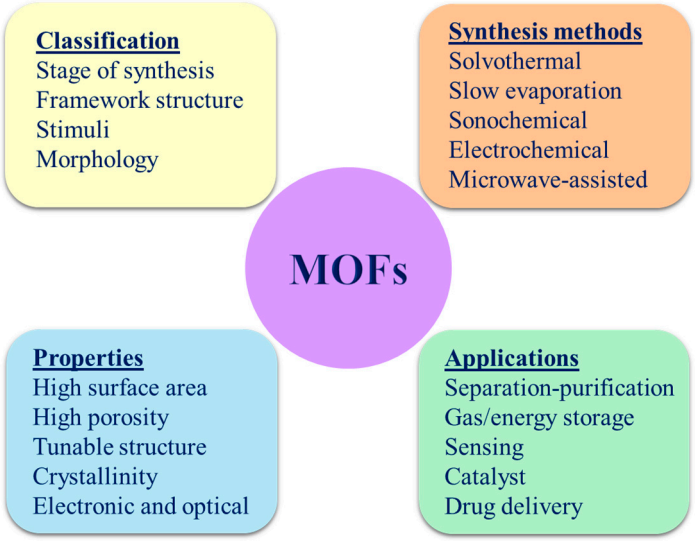

Figure 1. Schematic presentation of the classification, synthesis, properties, and applications of MOFs.

3.1. Fundamentals of MOFs for Photocatalytic Process

MOFs are popular materials in the environmental and clean energy fields because of their tunable structural advantages and chemical characteristics [33]. The selection of metal ions, organic linkers, and a proper solvent for their synthesis are critical factors in broadening their application in catalytic and clean energy processes. Using non-toxic metal ions, bio-based linkers, and green solvents are some of the primary approaches for this improvement [34].

The photocatalytic performance of MOFs includes absorption of light by the photosensitive units, formation and transfer of electron–hole pairs, and the subsequent redox processes on the surface of the photocatalyst (Figure 2). When light with proper intensity irradiates the catalyst, it leads to excitation of electrons to the conduction band, while leaving positively charged holes in the valance band [35]. Then, the excited electrons react with the dissolved oxygen, and holes react with water molecules to generate reactive radical species. These radicals contribute to the breakdown of organic contaminants [31]. The highly crystalline structure of MOFs enables a fast flow of electrons and energy from photo-excited MOFs to active sites in different photocatalytic reactions. The photocatalytic efficiency of MOFs depends on their organic linkers and the metal nodes. The organic linkers act as a photosensitizer, capturing photons and transferring the photogenerated electrons into the secondary building block (SBU). The metal nodes act as a direct semiconductor photocatalyst and charge-transfer system, increasing the movement of charge carriers. The nanoscale SBUs minimize charge recombination and prevent self-quenching [31]. Adjusting the bandgap of MOFs is a crucial factor in enhancing their performance as visible light active photocatalysts. Modifying linkers and doping with other metals can tune their bandgaps. The strategic design of MOF-based composite materials with bandgap engineering can improve their practical usage in environmental treatment [15].

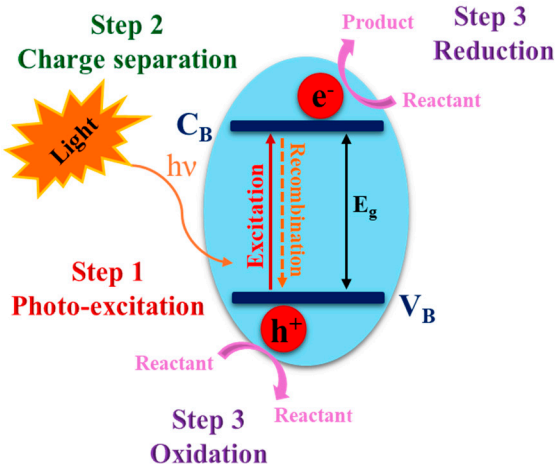

Figure 2. Schematic illustration of the photocatalytic process with MOFs. V_B and C_B denote the valence band and conduction band, respectively.

3.2. Functionalized MOFs

Functionalities introduced into different elements of the MOF structure consist of metal ions/clusters, linkers, and the vacant spaces within their cavities [36]. MOFs contain multiple functional linkers that can be pre-modified before synthesis of MOFs or post-synthesized. For example, various functional characteristics can be attained by modifying functional groups like -NH_2, -SO_3H, -OH, or -COOH on the benzene ring of linkers [22]. Most linkers are electron-rich and have intense absorption bands, which is tunable towards visible light by linker functionalization, metal ion immobilization, enzyme immobilization, and mixed metal/linker methods. Linker functionalization in MOFs can reduce their bandgap. MIL-125(Ti) is a UV-activated photocatalyst with a bandgap energy of 3.6 eV. Synthesis of NH_2-MIL-125(Ti) with 2-aminoterephthalic acid leads to a reduction in bandgap to 2.6 eV, which creates a visible light activated catalyst [37,38]. The synergistic effect of NH_2-MOFs improves their adsorption of opposite charged entities, molecule trapping, and interactions, exhibiting their effectiveness in diverse applications. Additionally, their responsiveness toward temperature, pH, and light irradiation expands their applications in photocatalysis and drug therapies [39].

The photocatalytic activity of functionalized MOFs can be modified at the molecular level by modifying the organic linkers to achieve hybridization or partial overlap

with the metal cluster's conduction band/valence band edge. Generally, in MOF-based photocatalysts, there are several photoexcitation pathways, consisting of ligand-to-ligand charge transfer, ligand-to-metal charge transfer, metal-to-metal-to-ligand charge transfer, and metal-to-ligand charge transfer [23].

Designing an effective photocatalyst relies on controlling the electron transfer processes to improve its performance [40]. Transition metals, with their delocalized electrons, can promote catalytic reactions. Also, preparing nanoscale materials maximizes the accessible active sites. Sometimes, these materials can agglomerate, resulting in reduced catalytic activity [41]. Incorporating silver or gold nanoparticles into UiO-66-NH_2 to create MNPs/UiO-66-NH_2 heterostructure effectively increases the visible-light photocatalytic efficiency of UiO-66-NH_2. The interface between MNPs and UiO-66-NH_2 promotes the separation of electrons and holes, enhancing quantum efficiency. Additionally, the pore confinement effect within UiO-66-NH_2 reduces the movement and aggregation of MNPs, resulting in higher stability [42]. Furthermore, MOFs can incorporate photosensitizers or catalytic components in their structure by immobilizing active sites on metal nodes or linkers or by encapsulating guest molecules within their pores.

3.3. Photocatalytic Activity of MOFs and Functionalized MOFs Towards Dye Pollutants

MOFs have several advantages for use in photocatalytic reactions: (1) the band structure and light absorption of MOFs are adjustable because of their flexible structure, (2) the porosity of MOFs offers more catalytic sites and enables the swift transport of reactants, and (3) the well-defined structure of MOFs is easily adaptable for the specific design of catalytic active sites, facilitating the study of catalytic mechanisms [15]. MOFs, as emerging eco-friendly catalysts, present noteworthy potential in eliminating organic contaminants in wastewater [22,31,43]. In theory, photocatalytic processes involve the excitation of a photocatalyst by light, which generates photoinduced charge carriers that engage in redox reactions [23]. Zhao et al. designed a new MOF, JUC-138, using In(III) and a pyrene-based linker, via a solvothermal method [44]. Crystallography results revealed that it crystallized in the monoclinic crystal system. In its structure, each In^{3+} is connected to four linkers in a bidentate chelate mode (Figure 3a–e), and its bandgap was calculated as 3.34 eV. JUC-138 could degrade 90% of Azure B (AB) dye within 4 h under UV light irradiation (Figure 3f).

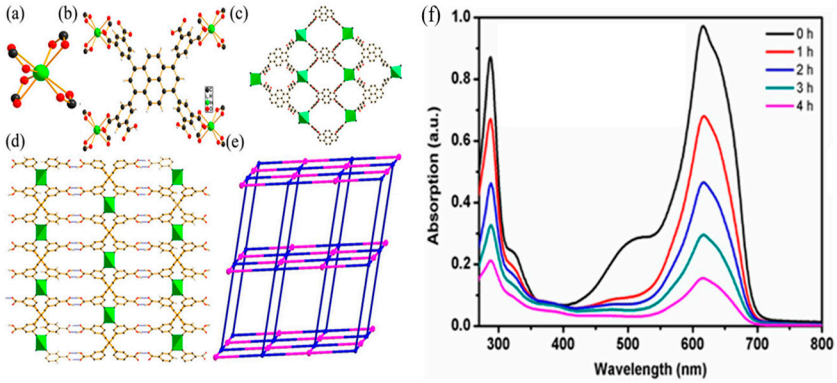

Figure 3. (**a**) Coordination geometry of In^{3+} and (**b**) coordination geometry of H8TIAPy in JUC-138. (**c**) 2D square sheet in direction [100], (**d**) hydrogen bonds constructed 3D supramolecular structure, (**e**) The tcj topology of JUC-138, (**f**) UV-vis spectra of photodegradation of AB solution with JUC-138. Adapted with permission from [44]. Copyright 2017 American Chemical Society.

Li et al. prepared UIO-66 and hydroxyl-modified UIO-66, named UIO-66-2OH(2,3), with a solvothermal method. BET-BJH measurements revealed the surface area of UIO-66 and UIO-66-2OH (2,3) as being 1050 $m^2\ g^{-1}$ and 570 $m^2\ g^{-1}$, respectively. The bandgap of UIO66-2OH (2,3) was calculated as 2.6 eV. UIO-66-2OH (2,3) could degrade 100% of methylene blue (MB) molecules upon exposure to visible light for 100 min. Its photocatalytic activity reached 99.5% after five cycles [45]. Jing et al. synthesized ZIF-8, [Zn(2-

methylimidazole)$_2$·2H$_2$O] under the slow evaporation method, using imidazolate as an organic linker. Its bandgap was calculated as 5.16 eV. BET surface area, and the total pore volume of ZIF-8 was measured as1799.6 m^2 g^{-1} and 0.6866 cm^3 g^{-1}. ZIF-8 degraded 82.3% of MB molecules in 120 min in the presence of UV light irradiation and followed a first-order kinetics model. ZIF-8 demonstrated enhanced activity in a strong alkaline condition resulting from the higher charged ZIF-8 (pH > pH$_{pzc}$ (pH in point of zero charge)) and the elevated yield of hydroxyl radicals facilitated by the increased hydroxide concentration [46].

MILs are a group of MOFs with excellent porosity, ultrahigh surface area, and numerous active sites. Furthermore, their surface activities, light response range, and charge separation effectivity are tunable [47]. The linkers in the MILs lattice can provide active chromophores for light absorption. At the same time, metal nodes act as isolated semiconductor quantum dots that can be activated with light irradiation. Generally, bare MILs can be directly used as photocatalysts. Interestingly, Fe-based MILs can be excited with visible light. MIL-53(Fe), constructed by 1,4-benzene dicarboxylic acid and Fe (III) metal clusters, is widely used in photocatalytic processes because of its visible light active iron–oxo clusters [47]. MIL-53(Fe) was prepared under a solvothermal reaction at 150 °C for 2 h. The bandgap of MIL-53(Fe) was calculated as 2.88 eV. MIL-53(Fe) completely degraded Rhodamine B (RhB) within 50 min in the presence of hydrogen peroxide and visible light [48].

In another study, Rezaei et al. synthesized MIL-53(Fe) by a solvothermal method at 150 °C overnight. Its bandgap was measured as 2.76 eV. SEM images showed hexagonal bipyramid morphology for MIL-53(Fe). Its surface area was calculated as 22.2 m^2 g^{-1}, with a pore size of 1.85 nm and pore volume of 0.041 cm^3 g^{-1}. TOC removal for photodegradation of MB with MIL-53 (Fe) was 58% under visible light irradiation [49].

MIL-100(Fe) is a rigid Fe-MOF with two types of permanent pores, and its water stability depends on aqueous pH and co-existing anions. MIL-100(Fe) acted as a Lewis acid, enhancing interactions with the target organic contaminants. The Fe–O clusters in MIL-100(Fe) can absorb visible light and generate electron–hole pairs, which enhance photocatalytic reactions [50]. Mahmoodi et al. synthesized MIL-100 (Fe) by a hydrothermal procedure, using trimesic acid as an organic linker. Various metal sources, including iron(III) chloride, iron(III) nitrate, and iron(III) sulfate, were used to produce MOFs with bandgaps of 5.41 eV, 5.44 eV, and 5.71 eV, respectively. The catalysts degraded Basic Blue 41 (BB41) following first-order kinetics. MIL-100(Fe) showed good photocatalytic activity over three catalytic cycles [51]. Similarly, MIL-100(Fe) was prepared at room temperature using benzene tricarboxylic acid as a linker. The estimated surface area of the MIL-100(Fe) was 1974 m^2 g^{-1} by BET. Its bandgap was calculated as 3.08 eV. MIL-100(Fe) degraded 64% of MO molecules in 7 h under UV light irradiation [52]. In another study, Xia et al. synthesized Cd-TCAA by the hydrothermal reaction at 110 °C for 2 days, using 4,4′,4″-tricarboxyltriphenylamine, and (E)-1,2-di (pyridin-4-yl) diazene as organic linkers. Cd-TCAA showed an efficiency of 81% for the degradation of MB within 175 min under visible light irradiation. The kinetic of the photocatalytic reaction was fitted to a first-order rate equation with rate constant of 0.01 min^{-1}. FT-IR, XRD and BET results confirmed its stability during photocatalytic reactions [53]. Li et al. synthesized a 3D Cu-MOF, {[Cu(L)$_{0.5}$ (H$_2$O)$_2$]$_4$H$_2$O}n (HPU-4) under solvothermal reaction at 80 °C for 72 h. It degraded only 20% of MB molecules in 60 min under visible light irradiation [54]. In another study, MIL-88A was prepared via a hydrothermal method at 65 °C for 12 h. SEM images showed hexagonal microrod morphology for MIL-88A. Its bandgap was 2.05 eV. MIL-88A could degrade only 12% of MB molecules in 80 min under visible light. The mechanism suggests •OH and •O_2^- as key species in the photodegradation process [55]. Abdi et al. synthesized UiO-66 and UiO-66-NH$_2$ with a solvothermal reaction at 120 °C for 24 h, using terephthalic acid and 2-aminoterephthalic acid as organic linkers, respectively. The bandgaps of UiO-66 and UiO-66-NH$_2$ were estimated to be 4.05 and 2.93 eV. By adding amine groups, the bandgap of UIO-66 decreased significantly, and UiO-66-NH$_2$ was a visible light active photocatalyst. The BET surface area of UiO-66 and UiO-66-NH$_2$ crystals

were 1120 m^2 g^{-1} and 1113 m^2 g^{-1}, respectively. The photocatalytic efficiency of UiO-66 and UiO-66-NH_2 for degradation of RhB under visible light irradiation was 42% and 60%, respectively, within 30 min [56]. In another study, Ao et al. synthesized Cu-doped NH_2-MIL-125(Ti). SEM images showed the undoped and Cu-doped NH_2-MIL-125(Ti) presented regular octahedron morphology. Doping of Cu facilitated effective electron trapping and reduced e^-/h^+ pair recombination. Cu-doped NH_2-MIL-125(Ti) could degrade 98.2% of MO molecules in 90 min under visible light. The rate constant of the 1.5 wt% Cu-NH_2-MIL-125(Ti) was 10.4-fold higher than NH_2-MIL-125(Ti). Also, it showed exceptional structural stability and high photocatalytic efficiency across four cycles [57]. Over the last decade, many studies have been carried out to integrate linkers with coordination networks of MOFs as a new technique for the development of efficient photocatalysts. MOFs with mixed linkers show multifunctional MOF characteristics such as designable topologies, tunable porosity and functionality, and different surface environments [58]. Jin et al. synthesized UiO-66-NO_2 (**1**), UiO-66-NH_2 (**2**), and UiO-66-NO_2/UiO-66-NH_2 (**3**) and studied their photocatalytic efficiency for the degradation of RhB solution. Under UV light irradiation, **1** and **2** only degraded 25% and 57% of RhB in 50 min, while **3** showed the best efficiency, with a degradation of 95.5%. Mixing linkers led to a reduction in the rate of hole–electron pair recombination and improved the photocatalytic efficiency and reusability of UiO-66-NO_2/UiO-66-NH_2 over the respective single component counterparts. The trapping experiments indicated $\bullet O_2^-$ as the main active species during the photocatalytic reaction [59].

The efficiency of MOFs has also been compared with common photocatalysts like TiO_2, ZnO, and SnO_2. TiO_2 is considered the most ideal semiconductor material due to its high stability, low cost, and its general consideration as an environmentally safe product. Rutile and anatase both have tetragonal crystal structures with bandgaps of 3.0 eV and 3.2 eV, respectively [60]. Duran et al. studied the photocatalytic degradation of dye pollutants using TiO_2 thin film. The estimated bandgap of the TiO_2 thin film was 3.24 eV. The comparison study showed it could degrade only 19.6% of MB molecules under UV irradiation [61]. In another study, TiO_2 nanoparticles were used for the degradation of MB under UV light irradiation. TEM images show uniform particles with sizes in the range of 25–30 nm. TiO_2 degraded 40% of MB molecules in 90 min [62]. In another study, SnO_2 was synthesized with a sol–gel method, followed by calcination at temperatures of 300–600 °C. The XRD pattern confirmed the successful synthesis of materials without impurities. TEM images demonstrated particle sizes of 6 to 15 nm for the synthesized SnO_2 nanoparticles. Its bandgap was in the range of 4.15 eV to 3.92 eV. Under UV-vis light irradiation, SnO_2 NPs degraded 93% and 86% of MB and RhB solution, respectively, within 90 min [63]. In a similar study, pure ZnO, SnO_2, and ZnO-SnO_2 nanostructures were prepared under a hydrothermal reaction at 230 °C for 12 h, followed by annealing at 700 °C for 8 h. The bandgaps of ZnO, SnO_2, and ZnO-SnO_2 were calculated as 3.37 eV, 3.6 eV, and 2.84 eV, respectively. All materials were used for the degradation of MB under visible light. The results revealed efficiencies of 38.5%, 32.7%, and 82.4% for ZnO, SnO_2, and ZnO-SnO_2, respectively, within 120 min. The enhanced photocatalytic activity of the ZnO-SnO_2 heterostructure is due to the high separation of charge carriers and the interface of the heterostructure. The results confirmed that synthesis of a heterojunction could improve the photocatalytic efficiency of bare metal oxides significantly [64]. For more details, the photocatalytic reaction condition and degradation efficiency of the discussed photocatalysts are summarized in Table 2.

Table 2. Comparison of the photocatalytic efficiency of MOFs with common metal oxides towards dyes.

Catalyst	Light Source	Dye	Dye Conc. (mg L^{-1})	Catalyst Dosage (mg mL^{-1})	Reaction Time (min)	Degradation (%)	Ref.
TiO_2	UV	MB	10	-	300	19.6	[61]
TiO_2	UV	MB	0.05 mM	1	90	40	[62]
SnO_2	UV-vis	MB	-	0.3	90	93	[63]
SnO_2	UV-vis	RhB	-	0.3	90	86	
ZnO	Vis	MB	10	0.1	120	38.5	[64]
SnO_2	Vis	MB	10	0.1	120	32.7	[64]
ZnO@SnO_2	Vis	MB	10	0.1	120	82.4	[64]
JUC-138	UV	Azure B	-	-	240	90	[44]
UIO-66-2OH	Vis	MB	-	-	100	100	[45]
ZIF-8	UV	MB	10	0.2	120	82.3	[46]
MIL-53(Fe)	Vis	RhB	10	4	50	100	[48]
MIL-100(Fe)	UV	MO	5	0.33	420	64	[52]
Cd-TCAA	Vis	MB	28 μM	0.1	175	81	[53]
HPU-4	Vis	MB	12.75	0.3	60	20	[54]
MIL-88A	Vis	MB	-	-	80	12	[55]
UiO-66	Vis	RhB	15	0.3	30	42	[56]
UiO-66-NH_2	Vis	RhB	15	0.3	30	60	[56]
NH_2-MIL-125(Ti)	Vis	MO	10	0.4	90	37	[57]
Cu-doped NH_2-MIL-125(Ti)	Vis	MO	10	0.4	90	98.2	[57]
UiO-66-NO_2 (**1**)	UV	RhB	10	1	50	25	[59]
UiO-66-NH_2 (**2**)	UV	RhB	10	1	50	57	[59]
UiO-66-NO_2/UiO-66-NH_2 (**3**)	UV	RhB	10	1	50	95.5	[59]

3.4. Effect of Various Parameters on the Photodegradation of Dyes with MOFs

3.4.1. Light Source

In the photocatalytic processes, the intensity and wavelength of light, as well as the irradiation time, play important roles. The light intensity affects the catalytic reaction rate by enhancing the excitation of the photocatalyst and generation of electron–hole pairs. Additionally, the wavelength of irradiation can affect the electronic and optical properties of the catalyst, some catalysts requiring UV irradiation while others functioning using visible light [65]. Accordingly, the bandgap energy is an important parameter that needs to be determined and reported for each developed photocatalyst.

3.4.2. Initial Concentration of Dye Solution

Generally, the efficiency of the photocatalyst decreases as the initial concentration of the dye solution increases, because it may lead to a higher concentration of the intermediate species resulting in competition between the dye molecules and the intermediate species for the active sites. Blockage of the active sites of the catalyst leads to low catalytic efficiency. Furthermore, a high concentration of dyes can hinder the light permeability and decrease the photocatalytic efficiency [65,66]. For example, the effect of increasing the concentration of dye in the photocatalytic process was studied with ZnO@HKUST-1, by keeping the catalyst dosage fixed and varying the initial concentration of RB (20–80 mg L^{-1}). Under sunlight irradiation, the highest efficiency of 97.4% within 45 min was reported for RB solution with a concentration of 20 mg L^{-1}. Upon further increasing the dye concentration, the catalytic activity of the composite material decreased due to blockage of the catalyst active sites by dye molecules. Furthermore, the dye molecules absorb light, limiting it from reaching the catalyst surface and leading to reduced catalytic activity [67].

3.4.3. Initial pH of Dye Solution

The initial pH of the dye solution plays an important role in controlling photocatalytic reactions. It can affect the photocatalytic reaction by changing the charge of the photocatalyst surface and influencing particle aggregation. Furthermore, the acidity of

the solution influences the electrostatic interactions between the surface of photocatalyst, solvent molecules, and charged reactive species [24,65]. The pH_{PZC} of the catalyst is influenced by solution pH, and reporting zeta potential values enables the proper evaluation of newly developed photocatalyst materials. At pH close to the pH_{PZC}, the charge of the catalyst is near neutral, minimizing broad electrostatic forces. At pH values either below or above the pH_{PZC}, the catalyst has a net charge, which can attract or repel charged dye molecules [65].

3.5. Stability and Regeneration of MOFs

While MOFs have remarkable potential for photocatalytic applications, there are some challenges regarding their stability and regeneration. Much research has been done to address these challenges by developing synthetic methods and structural modifications of MOFs [34]. Chemical stability and regeneration of MOFs affect their efficiency in environmental applications [33].

The chemical stability of MOFs can be tuned by modifying the linkers, metal ions, and reaction conditions. The strength of metal–ligand bonds of MOFs plays an important role in their stability. According to Pearson's hard and soft acids and bases principle, MOFs with suitable metal–linker pairs show high stability in catalytic reactions. Furthermore, the pH of the reaction solution can affect the chemical stability of MOFs [16,34]. Combination of carboxylate-based linkers, as hard base, with high-valent, hard acid metal ions like Zr^{4+}, Fe^{3+}, Al^{3+}, and Ti^{4+} can lead to the synthesis of stable MOFs. Ti^{4+} and Zr^{4+} require more ligands to balance their charges, leading to higher connectivity and greater stability. Also, surface modification that increases its hydrophobicity reduces the impact of water molecules on the internal MOF structure. Therefore, increasing hydrophobicity of MOFs via post-modification is another method to improve their chemical stability, which includes linker functionalization and surface coating. Hence, designing a suitable MOF according to the conditions of the catalytic reaction process is an important step and should be considered when using MOFs in challenging solution environments [16,33]. Furthermore, the synthesis of composite materials is another good option to improve the catalytic efficiency and recyclability of MOFs.

4. Photocatalytic Activity of MOF-Based Composite Materials

MOFs with high porosity and significantly high surface areas are excellent hosts for loading guests. These composite materials improve and expand the usage of MOFs in different fields [68]. A composite material is a combination of two or more different substances that retain their characteristics while improving the properties of the overall system [68,69]. Several functional materials have been used for synthesizing composite materials with MOFs, with some of the common materials being polymeric materials [70,71], porphyrins [72,73], graphene oxide [28], graphitic carbon nitride [74,75], carbon quantum dots [76], metal nanoparticles [77,78], metal oxides [79,80], and metal chalcogenides [81,82]. Generally, MOF-based composite materials are classified into five main groups: metal–MOFs, nonmetal–MOFs, bio–MOFs, polymer–MOFs, and semiconductor–MOFs [11]. Moreover, the critical parameter for applying MOFs on a large scale is their stability and reusability, particularly in water [83]. Composite materials reveal significant advantages in chemical and physical properties such as mechanical strength, conductivity, stability, and catalytic activity [1]. Composites of MOFs with semiconductors has a synergistic effect and decreases the drawbacks of both materials. In heterojunction systems, MOFs act as electron trappers, reducing electron–hole recombination while holes remain in the semiconductor surface, both assisting in reactive species generation [11,23]. Furthermore, the porosity and high surface area of MOFs facilitate the dispersion of the incorporated semiconductors, which prevents the aggregation of semiconductors and increases the number of available active sites [1].

4.1. Metal-MOF Composite Materials

The goal of combining MOF with metal nanoparticles is generally to enhance the physicochemical properties of one or both constituents [11]. Liaqat et al. constructed Ni-MOF using 4-methyl thiophene-2-carboxylic acid as an organic linker under reflux reaction. Mo-doped Ni-MOF composite materials (Mo@Ni-MOF) were prepared using the same technique. The reduced bandgap from 1.96 to 1.83 eV for Mo@Ni-MOF revealed that the composite material can potentially suppress the recombination of carriers. EDX and elemental mapping analyses confirmed the presence of Mo in the composite materials. Introducing Mo into Ni-MOF resulted in a superior MB degradation, with an efficiency of 84%, compared to pure Ni-MOF (68%) within 70 min under solar light irradiation. The scavenger experiments identified superoxide anion radicals as key species in the photodegradation reaction. Mo@Ni-MOF showed high stability and reusability after four successive runs [40]. In another study, Cu@MOFs were synthesized using the incipient wetness impregnation method. The effect of Cu loading on synthesized MOFs containing MIL-100(Fe), NH_2-MIL-53(Al), Zr-BDC, and NH_2-Zr-BDC was studied. The composite materials were used for photodegradation of RhB under visible light irradiation. The impregnation of Cu induces a slight decrease in the bandgap in all MOFs. Cu_2@NH_2-Zr-BDC (with 2 wt% Cu loading) showed the best results in the degradation of RhB, with an efficiency of 93%, upon exposure to visible light for 170 min. Scavenger tests suggested holes as the most active species in the photocatalytic process [77].

Ag@MOF-801/MIL-88A(Fe) nanocomposite was synthesized through template effects in MOFs. The bandgaps of MOF-801, MOF-801/MIL-88A(Fe), MIL-88A(Fe), and Ag@MOF-801/MIL-88A(Fe) were calculated as 4.4 eV, 2.8 eV, 2.66 eV, and 2.6 eV, respectively. The nanocomposite showed the highest efficiency of 91.7% for the degradation of Reactive Black 5 after 30 min under visible light irradiation. AgNPs demonstrate surface plasmon resonance (SPR) that leads to reduction of electron–hole recombination. Additionally, MIL-88A(Fe) has a photo-Fenton effect that can improve the photocatalytic activity of the nanocomposite. The main active species in the photocatalytic degradation were hydroxyl radicals and holes [78]. Gua et al. synthesized Ag@MOF-525 composite materials by a photoreduction method using porphyrin-based MOF. The synthesis scheme of the composite material is shown in Figure 4a. The BET surface areas of MOF-525 and Ag@MOF-525 were measured as 2690 $m^2\ g^{-1}$ and 2247 $m^2\ g^{-1}$. XRD, HRTEM, and UV-DRS analyses demonstrated the successful loading of singlet Ag. Furthermore, XPS analysis of Ag@MOF-525 confirmed the presence of C, N, O, Zr, and Ag in a manner consistent with the SEM mapping images. The composite demonstrated higher photocatalytic activity than MOF-525; it degraded 91% of RhB molecules in 60 min and 81% of tetracycline (TC) in 200 min under visible light. Ag serves as an electron trap, leading to effective suppression of electron–hole recombination, enhancing the electron transfer and improving the photocatalytic activity of Ag@MOF-525 (Figure 4b). The trapping experiments indicated that h^+ and $\bullet O_2^-$ are the main active species for the photocatalytic reaction [72].

In another study, Ag@MIL-125(Ti) was synthesized by a hydrothermal reaction, following photo-reduction. TEM images demonstrated that AgNPs with a diameter of 40 nm are dispersed on MIL-125(Ti) microspheres. The presence of AgNPs in the structure of the composite material enhanced visible light absorption significantly. Ag(3 wt%)@MIL-125(Ti) showed the highest efficiency, with complete degradation of RhB in 40 min. Scavenger experiments indicated that $\bullet O_2^-$ and •OH were the main reactive species. The catalyst was reused for five cycles without significant changes in its catalytic performance [84]. ZIF-8 was prepared using 2-methylimidazole as a linker, at room temperature. Ag-X@ZIF-8 composite materials with different silver contents were synthesized by photo-irradiation. The elemental mapping analysis of Ag@ZIF-8 confirmed a uniform distribution of C, N, Zn, and Ag elements. The bandgaps of the ZIF-8 and Ag-doped ZIF-8 were estimated at around 5.44 eV and 3.2 eV. SEM and TEM images showed that ZIF-8 displayed the rhombic dodecahedron morphology, and the composite materials showed the same morphology as ZIF-8. Among the synthesized catalysts, Ag-15%@ZIF-8 showed the best result, with 100%

and 93% efficiency for methyl orange (MO) and RhB, respectively, in 30 min under visible light irradiation. The composite material maintained its photocatalytic performance after four cycles. Trapping studies indicated that hydroxyl radicals and photo-generated holes are the main active species in the photocatalytic elimination of both dyes [85]. In a similar study, Chandra et al. synthesized multi-core-shell AgNPs@ZIF-11 by in situ encapsulation of AgNPs in ZIF-11. ZIF-11 was prepared by stirring at room temperature, using benzimidazole as an organic linker. The composite materials AZ1, AZ2, and AZ3 were synthesized with 150, 300, and 500 µL, respectively, of AgNPs suspensions (1 mg of AgNPs dispersed in 2 mL methanol). Encapsulation of AgNPs (particle size: 11.8 ± 2.3 nm) was confirmed by TEM. XPS spectra and mapping images confirmed the presence of AgNPs in the AZ1 composite material. The UV-DRS spectra showed the lowering of the bandgap of ZIF-11 from 4.36 eV to 4.21 eV for AgNPs@ZIF-11. AZ1 exhibited excellent photocatalytic activity (almost 100%) toward MB molecules under UV–visible light irradiation. The AZ1 was reused for up to three cycles with the same efficiency of 100%. Scavenger analysis revealed that h^+ and •OH played an important role for the photocatalytic reaction [86]. Ag/UiO-66-NH_2 composite materials were synthesized in two steps, involving wet impregnation of silver nitrate into UiO-66-NH_2, followed by chemical reduction with sodium borohydride. TEM images of Ag/UiO-66-NH_2-30% showed that the spherical AgNPs, with sizes of less than 10 nm, are well dispersed throughout the UiO-66-NH_2. Ag/UiO-66-NH_2-20% could degrade 96.4% of RhB in 40 min under UV–vis light and in the presence of hydrogen peroxide. The composite material exhibited higher photocatalytic performance in comparison with bare MOF (74.3%). The enhanced photocatalytic activity of composite materials can benefit from the built-in heterostructures that can increase the electron–hole separation and the absorption of the visible light. Ag/UiO-66-NH_2 demonstrated good reusability with a slight drop in efficiency after three consecutive runs [42]. For more details, the photocatalytic reaction condition and efficiency of the discussed metal@MOF composite materials is listed in Table 3.

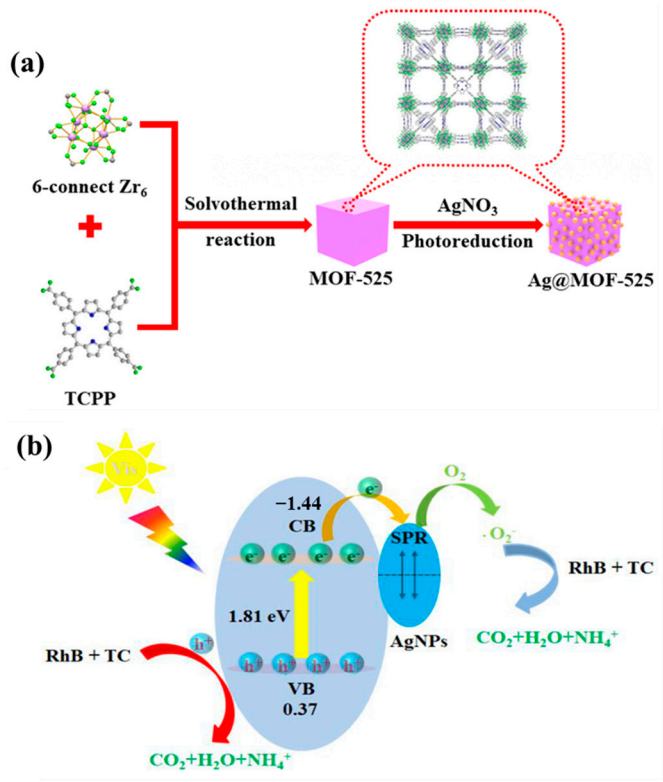

Figure 4. (**a**) The synthetic route of composite catalyst Ag@MOF-525 and (**b**) diagram of the degradation process. Adapted with permission from [72]. Copyright 2023 Elsevier.

Table 3. Comparison of the photocatalytic efficiency of metal@MOF composite materials towards dye pollutants.

Catalyst	Light Source	Dye	Dye Conc. (mg L^{-1})	Catalyst Dosage (mg mL^{-1})	Reaction Time (min)	Degradation (%)	Ref.
Ni-MOF	solar	MB	10	0.2	70	68	[40]
Mo@Ni-MOF	solar	MB	10	0.2	70	84	[40]
Ag@MOF-525	Vis	RhB	20	1	60	91	[72]
Ag@MIL-125(Ti)	Vis	RhB	-	1	40	100	[84]
Ag@ZIF-8	Vis	MO	15	0.8	30	100	[85]
	Vis	RhB	15	0.8	30	93	
AgNPs@ZIF-11	UV-vis	MB	1.6	-	40	100	[86]
Ag/UiO-66-NH_2	UV-vis	RhB	2×10^{-5} mol L^{-1}	0.33	40	96	[42]

4.2. Nonmetal–MOF Composite Materials

Carbon-based materials, including carbon nanotubes, graphitic carbon nitride, graphene-based materials, and MXene, are commonly used for developing composite materials. Carbon-based materials show excellent light absorption, high conductivity, and stable structure. Since some MOFs suffer from poor conductivity and low stability, composing MOFs with carbon-based materials is a key solution to overcome these drawbacks of pristine MOFs [15,87]. Quang et al. synthesized bismuth–MOFs@carbon nanotube, labelled as BiBTC@CNTs (BTC: trimesic acid, CNT: carbon nanotube), using a microwave-assisted solvothermal procedure. SEM images showed a rod-shaped morphology for BiBTC, while BiBTC@CNTs retained the rod-shaped morphology of MOF, interwoven with the fiber structure of the CNT. The bandgap of BiBTC and BiBTC@CNTs-2 were calculated as 3.7 eV and 3.5 eV, respectively. BiBTC@CNTs-2 showed the best results, with a degradation efficiency of 98% toward RhB in 180 min under visible light. The increased separation of electron–hole pairs via a built-in electric field in the composite material was a key factor enhancing photocatalytic efficiency. The superoxide anion radicals and electrons played crucial roles in the photodegradation of RhB [88]. Porous g-C_3N_4 was fabricated using thermal polymerization and used to synthesize g-C_3N_4/UiO-66 (CNU) composite materials. The g-C_3N_4 nanosheets were grown onto UiO-66 to synthesize composite materials. The bandgaps of UiO-66, g-C_3N_4, and CNU-0.5 were calculated as 3.96 eV, 2.88 eV, and 2.92 eV, respectively. CNU-0.5 degrades 100% of RhB solution upon exposure to visible light for 70 min, which was 6.46- and 10.56-fold faster than that of pure g-C_3N_4 and UiO-66, respectively. The formation of a heterojunction improved the photoelectron transfer and reduced the electron–hole recombination. Scavenger studies revealed $\bullet O_2^-$, h^+, and •OH as active species in this reaction [89]. Zhang et al. prepared MIL-101(Fe)/Ce/g-C_3N_4 (MCCN) composite materials with different molar amounts of Ce/g-C_3N_4 (Figure 5a). The bandgap values of Ce/g-C_3N_4, MIL-101(Fe), MCCN-1, MCCN-3, and MCCN-5 were reported as 2.50 eV, 2.46 eV, 2.40 eV, 2.34 eV, and 2.48 eV, respectively. The introduction of Ce/g-C_3N_4 decreased the bandgap and enhanced the absorption of visible light in the composite material. SEM images (Figure 5b,c) showed octahedral and 2D layered morphologies for MIL-101 (Fe) and Ce/g-C_3N_4, respectively. The SEM image of MCCN-3 (Figure 5d) demonstrated that g-C_3N_4 layers covered the surface of octahedral MIL-101(Fe) particles. The optimum photocatalyst (MCCN-3) exhibited the highest performance, degrading 90.36% of RhB and 88.17% of MB molecules in 75 min of exposure to visible light. The results are shown in Figure 5f,g. The enhanced light absorption, formation of a heterojunction, and effective electron–hole transfer enhanced the photocatalytic performance of the composite material [90].

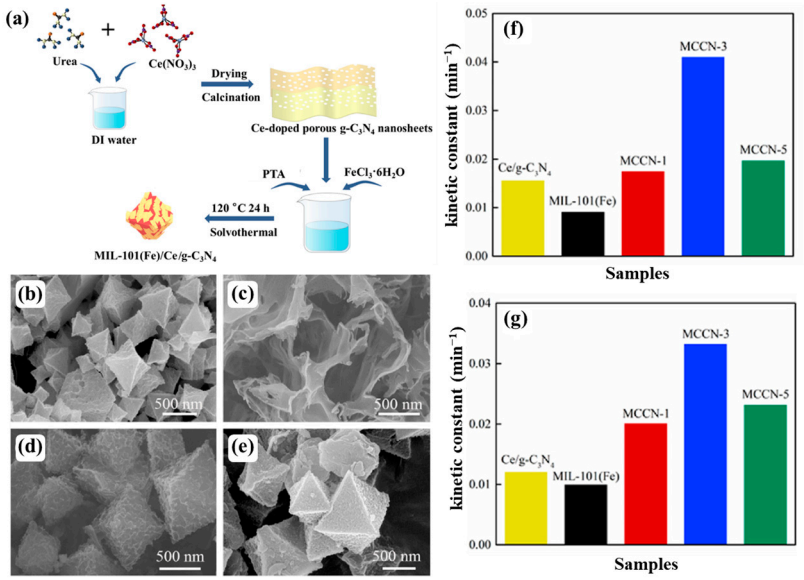

Figure 5. (**a**) Schematic illustration for synthesis of composite material; SEM images of (**b**) MIL-101(Fe); (**c**) Ce/g-C_3N_4; (**d**) MCCN-3; (**e**) MCCN-5; and (**f**,**g**) kinetics study of catalysts for elimination of RhB and MB, respectively. Adapted with permission from [90]. Copyright 2023 Elsevier.

Ce-MOF/g-C_3N_4 (Ce-CN) composite materials were developed by in situ deposition of Ce-MOF onto g-C_3N_4. Ce–CN-TS (solvothermally treated carbon nitride) exhibited a bandgap of 2.45 eV. The photocatalytic performance of the Ce–CN-TS composite material was remarkably superior to bare materials, achieving a 96.5% elimination of MB upon exposure to UV–visible light for 120 min, its degradation efficiency decreasing to 80.5% by the fourth cycle [91]. MOF-5 was synthesized by stirring at room temperature and used to develop composite materials with graphene oxide (GO). The MOF-5/GO5 and MOF-5/GO10 composites containing 5% and 10% weight fractions of GO were prepared. The photocatalytic elimination of MB was 64% for MOF-5, 85% for MOF-5/GO5, and 92% for MOF-5/GO10 over 390 min under UV light. The MOF and graphene oxide composition reduced electron–hole recombination and enhanced charge transfer. The reactive oxygen species $\bullet O_2^-$, $HO_2\bullet$, and •OH were the main contributors to the photocatalytic activity [28].

Recently, graphene quantum dots (GQDs) have gained much attention in various usages due to their nano size, photostability, non-toxicity, and biocompatibility. Mukherjee et al. synthesized MIL-100(Fe)/GQD composite materials using GQD and MOF precursors. The bandgaps of MIL-100(Fe) and the composite material were 2.35 eV and 1.93 eV, respectively. MIL-100/GQD showed a maximum efficiency of 93.8% within 5 min for degradation of Congo Red (CR) under visible light irradiation. Incorporating GQD increased charge separation in the composite material, which was confirmed by photoluminescence (PL) spectra. The trapping experiment demonstrated h^+ and $\bullet O_2^-$ as the active species in the degradation of CR. The composite material exhibited appreciable reusability after four cycles [92]. Carbon quantum dots (CQDs) are excellent fluorescent nanomaterials with exciting properties, including small particle size, high fluorescence stability, broad excitation spectrum, good biocompatibility, and low toxicity [93]. CQDs can be electron receptors, photosensitizers, or spectral converters in photocatalytic systems. Furthermore, doping CQDs with nonmetallic elements, like nitrogen, can improve their optical stability, electron transferability, and catalytic activity [76]. Rahmani et al. synthesized composite materials with MIL-101(Cr) (MIL-Cr) and nitrogen-doped carbon quantum dots: MIL-Cr/N-CQDs(x) (x = 0.5, 1, 2, and 3 mL of N-CQDs solution). EDX and mapping analyses confirmed the presence of C, N, O, and Cr in MIL-Cr/N-CQDs (2). The bandgap was 2.58 eV for MIL-Cr and 1.95 eV for MIL-Cr/N-CQDs (2). HR-TEM images confirmed the distribution of N-CQDs on the surface of MIL-Cr in the composite material. MIL-Cr/N-CQDs (2) composite exhibited the highest photocatalytic performance toward RhB (95% in

160 min) in the presence of visible light and hydrogen peroxide. In the composite material, N-CQDs act as electron acceptors, increasing the visible light absorption and preventing fast electron–hole recombination. Scavenging experiments showed that hydroxyl radicals and holes were crucial for photodegradation. The degradation efficiency of the composite material reached 75% within three cycles [76]. Chen et al. developed (UNiMOF/Ti_3C_2; UNT) composite materials using the sonochemical method. SEM images demonstrated 2D sheet-like and 2D flower-like nanosheets for Ti_3C_2 MXene and UNiMOF, respectively. The TEM image of UNT1.5 demonstrated a uniform adherence of UNiMOF nanosheets on Ti_3C_2 nanoflakes. The UNT1.5 (with 1.5 wt% Ti_3C_2) achieved the highest efficiency of 99.5% for degradation of MB within 120 min, which was four times that of UNiMOF. The 2D structures and the high conductivity of Ti_3C_2 enhanced electron–hole separation, resulting in improved photocatalytic performance. The scavenger experiments revealed •OH as the main active species, while $\bullet O_2^-$ and h^+ participate in the photodegradation reaction [94].

4.3. Bio–MOF Composite Materials

Bio–MOF composite materials contain at least one biomolecule serving as an organic ligand. Incorporating biomolecules into MOFs can improve their durability and expand their capabilities. The effectiveness of MOFs could be enhanced by adding biomolecular entities like saccharides, nucleobases, proteins, peptides, amino acids, and porphyrins [95]. Porphyrins are effective photosensitizers known for their high light absorption capacity, long excited state lifetimes, and excellent stability [96]. Tetra(4-carboxyphenyl) porphyrin (TCPP) is the most common porphyrinic linker used in the synthesis of porphyrin-based MOFs (PMOFs) [97]. Chen et al. synthesized a new MOF via the solvothermal method; X-ray crystallography data revealed its structural formula as $[Me_2NH_2][Sr_2(TCPP)(OAc)(H_2O)]\cdot 2DMA$ [1, H4TCPP = tetrakis(4-carboxyphenyl) porphyrin, DMA = N,N′-dimethylacetamide, HOAc = acetic acid]. Its structure consisted of an anionic host framework and $Me_2NH_2^+$ counter cations. The MOF degraded 99% of RhB within 3 h and 99% of MB molecules within 22 min. The electrostatic interactions assisted in the adsorption of cationic dyes into the pores, while the porphyrin group provided singlet oxygen and superoxide anion radicals under light irradiation, leading to efficient elimination of dyes [73]. Three-dimensional TiO_2@Cd-MOF nanocomposite aerogels were synthesized through the sol–gel method and used for the synthesis of (TiO_2@Cd-MOF)@ZnPp with Zn(II) porphyrin (ZnPp). The bandgap values were reported as 3.0 eV, 2.9 eV, and 2.5 eV for pure TiO_2 aerogel (TAG), nanocomposite aerogel (TAC), and porphyrin-sensitized nanocomposite aerogel (PTAC), respectively. (TiO_2@Cd-MOF)@ZnPp achieved a maximum degradation efficiency of 94.1% toward MO molecules within 90 min upon exposure to visible light. The synergistic effects of heterostructure, increased optical absorption, and efficient electron injection lead to enhanced photocatalytic performance. These results showed that superoxide anion radical and hydroxyl radicals played key roles, whereas holes have minor roles in the degradation process [98].

Two-dimensional (2D) MOFs with ultra-thin structures provide a large surface area, more active sites, and shorter diffusion distances for heterogeneous catalytic reactions, producing higher photocatalytic performance than 3D MOFs [96,99]. A series of 2D M (Cu, Zn, Co, and Mn)-TCPP MOF were synthesized using tetrakis(4-carboxyphenyl) porphyrin (TCPP) linker. The synthesized MOFs were used for designing M-TCPP MOF/TiO_2 (MMOF-Ti) composite materials using a solvothermal reaction. 2D CuMOF-Ti-3 (synthesized using 300 µL of n-butyl titanate) exhibited the best photo-Fenton performance, with efficiency of 97.4% for the degradation of RhB within 30 min under visible light irradiation. The scavenger tests revealed the effect of active species is in the order of $h^+ > \bullet O_2^- >$ •OH. The composite material maintained its photocatalytic activity after five runs [96].

4.4. Polymer–MOF Composite Materials

The poor stability and low conductivity of MOFs restrict their photocatalytic usages. To address these drawbacks, polymeric materials, including polyaniline (PANI), polypheny-

lene vinylene, polypyrrole, polyethylene glycol (PEG), polyvinylidene fluoride (PVDF), polyether sulfone (PES), and chitosan, have been introduced. PANI has recently been noted in photocatalysis due to its high chemical stability, superior optical and mechanical properties, and high conductivity [2]. Furthermore, the ability to coat MOFs with polymeric materials and prepare them in beads, pellets, and hydrogel can expand their usage range. This adaptability in their structural forms facilitates their broad application in large-scale wastewater remediation.

The composition of polymers with MOFs has attracted significant attention because of synergistic advantages that include higher stability, activated functionalities, and improved catalytic efficiency. Wang et al. prepared MIL-101(Fe)/polysulfone (MP) composite material with the Pickering emulsion template technique (Figure 6a). UV-DRS spectra showed bandgaps of 2.62 eV for MIL-101(Fe), 3.76 eV for polysulfone (PSF), and 2.55 eV for MP-0.56. SEM images revealed homogeneous hollow microsphere composite materials. The MP-0.56 composite material achieved 100% removal of MB in 60 min under visible light, outperforming the pure materials. The porosity and electrostatic interaction between dye molecules and PSF resulted in improved photocatalytic activity of the composite materials. Trapping experiments and ESR analyses confirmed that •OH and $\bullet O_2^-$ species were critical in the catalytic process (Figure 6b,c). MP-0.56 maintained a removal efficiency of 91% after five cycles [100]. The suggested mechanism for the photocatalytic reaction using MIL-101(Fe)/ PSF is inserted in Figure 6d.

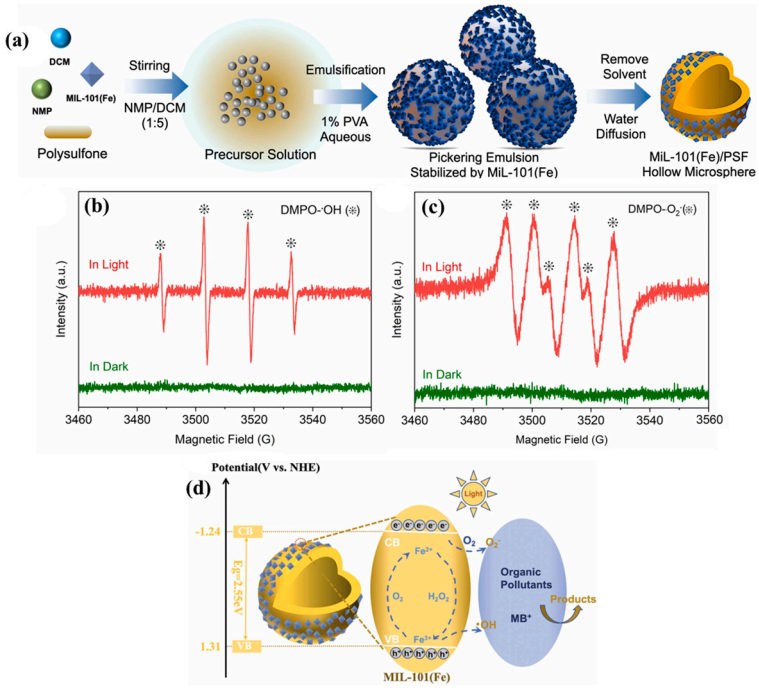

Figure 6. (**a**) Preparation scheme of MIL-101(Fe)/polysulfone composite materials; (**b**,**c**) ESR spectra of DMPO-•OH, TEMPO-•O_2; and (**d**) suggested mechanism of the photo-Fenton reaction for MB elimination using MIL-101(Fe)/PSF. Adapted with permission from [100]. Copyright 2023 Elsevier.

MOF/polymer composite materials were synthesized by incorporating MIL-100(Fe) and MIL-88A(Fe) into a polymer matrix via photopolymerization. The bandgap of 1%MIL-100(Fe)/polymer and 1%MIL-88 A(Fe)/polymer was calculated as 2.5 eV and 2.3 eV, respectively. The MOF/polymer composites degraded 95.2% of Acid Black (AB) molecules in 30 min under UV–visible light irradiation, while the efficiency of the bare polymer was only 35%. Furthermore, MIL-100(Fe)@polymer showed better performance than MIL-88A(Fe)/polymer. The suggested mechanism for the photodegradation of AB revealed that the dissolved oxygen was the key species. However, superoxide anion radical, hydroxyl, oxygenated, and carbonated radicals were also involved in this process. The composite

materials displayed excellent photocatalytic performance and stability for up to five cycles [101]. In a similar study, MIL-53(Cr) and HKUST-1(Cu) were synthesized under the solvothermal method and used to prepare MOF/polymer composite materials. The 2%MIL-53(Cr)/polymer showed the smallest bandgap of 2.1 eV. The 2% MIL-53(Cr)/polymer and 2%HKUST-1(Cu)/polymer composites degraded 96% of Acid Black (AB) in 30 min and 45 min, respectively, upon exposure to UV light irradiation. These photocatalysts showed a decrease in efficiency beyond the seventh cycle [102]. Fe-MIL88/microcrystalline cellulose composite material (Co, Fe-MIL88/MCC) was synthesized under stirring conditions (Figure 7a). Co, Fe-MIL88 and Co, Fe-MIL88/MCC composite materials showed bandgaps of 2.28 eV and 2.26 eV, respectively. SEM and TEM images of Co, Fe-MIL88/MCC revealed that the hexagonal rod-like morphology of MIL88 was preserved in the composite materials (Figure 7b). XRD and FT-IR spectra confirmed the successful synthesis of composite material. The composite material degraded 87% of RhB in 100 min under visible light, which was higher than for Co, Fe-MIL88 (61.75%). Trapping experiments and ESR analysis indicated that the photo-induced $\bullet O_2^-$ and •OH play key roles in the photocatalytic reaction. The photocatalytic reaction mechanism with the composite material is inserted in Figure 7c. The composite materials demonstrated good durability and reusability for up to five cycles [103].

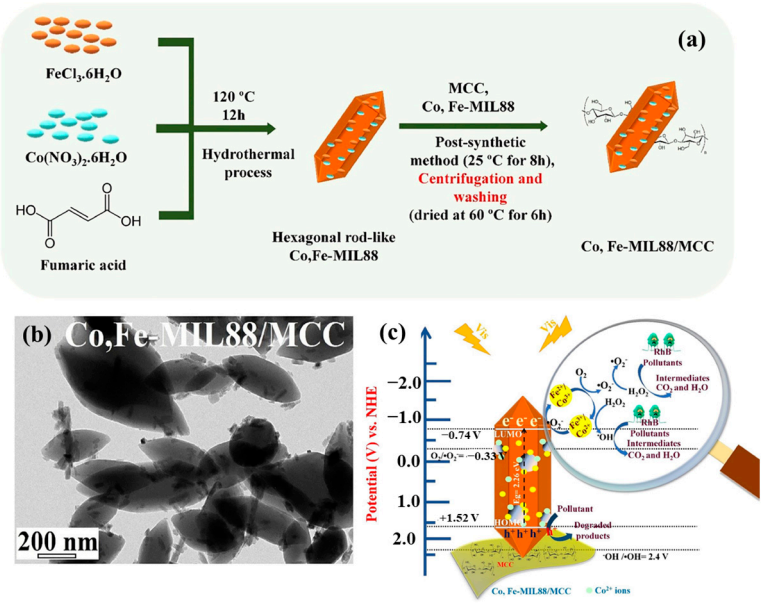

Figure 7. (**a**) Synthetic scheme of Co, Fe-MIL88/MCC; (**b**) TEM image of Co, Fe-MIL88/MCC; and (**c**) illustration of the photocatalytic reaction mechanism for the composite material. Adapted with permission from [103]. Copyright 2023 Elsevier.

MIL-53(Fe)/polyaniline (PANI) composites were synthesized by in situ depositing PANI onto MIL-53(Fe). The composite material simultaneously degraded RhB and Cr(VI) under pH = 2 with an efficiency of 98% in 200 min under UV-vis light irradiation. EIS, photocurrent response, and transient absorption spectra revealed that the photogenerated carriers have a longer lifetime in MIL-53(Fe)/ PANI than bare MIL-53(Fe). Scavenger experiments indicated $\bullet O_2^-$ and •OH as the main active species [104]. In a similar study, the polyacrylonitrile–polyaniline 2-methylimidazole zinc salt (PAN-PANI-ZIF8) fiber membranes were prepared by doping ZIF-8 with PAN and PANI matrices under an electrospinning method. The bandgap values were determined as 2.75, 5.48, and 2.74 eV for PAN–PANI-20, PAN–ZIF8-10, and PAN–PANI-20–ZIF8 fibers, respectively. The composite materials showed good efficiency in comparison with bare materials for the degradation of CR under visible light irradiation. The rate constant of the PAN–PANI-20–ZIF8 fiber (17.2×10^{-3} min^{-1}) was 13.2-fold faster than that of the PAN–PANI-20 fiber and 3.1-fold

higher than that of the PAN–ZIF8-10 fiber. The molecular dynamics simulation calculations verified that PANI, rather than PAN, strongly interacted with ZIF8 [26].

Niu et al. prepared ZIF-8/PAM (polyacrylamide) hybrid material through the recrystallization of ZnO/PAM precursors solvothermally [71]. The ZIF-8/PAM composite material degraded 88.6% of MB molecules within 30 min under visible light irradiation, while the efficiency of ZIF-8 was 82.3% in 120 min. Trapping experiments indicated that •OH and $\bullet O_2^-$ were the main active species in this reaction. UiO-66 was synthesized under solvothermal reaction conditions and used for the synthesis of (CS/UiO-66) composite materials using chitosan (CS). SEM images showed a sheet-like morphology and rhombic-shaped crystals for chitosan and UiO-66, respectively, while for CS/UiO-66, the SEM images indicated uniform, rhombic-shaped crystals. The maximum degradation efficiencies were observed as 75–95% for MB and MO (with initial concentration up to 2000 mg L^{-1}) using CS/UiO-66 in the presence of UV light irradiation and hydrogen peroxide. The efficiency of the CS/UiO-66 was 5–10 times higher than bare materials [70].

4.5. Semiconductor–MOF Composite Materials

Light absorption in semiconductors generates electron–hole pairs that enable separated oxidation and reduction of pollutants on their surface [92]. Metal oxides are suitable catalysts for wastewater remediation because of their photostability, effective charge carrier transfer, low cost, and efficient photocatalytic performance. Roy et al. synthesized ZnO@HKUST-1 composite material with a chemical precipitation method and further calcination. The bandgaps of HKUST-1, ZnO, and ZnO@HKUST-1 were 3.2 eV, 3.1 eV, and 2.72 eV, respectively. SEM images revealed that the octahedral shape of the HKUST-1 remained intact in the nanocomposite material. The composite material exhibited an excellent efficiency of 97.4% in 45 min for Rose Bengal (RB) degradation under sunlight. Scavenger tests demonstrated that •OH and $\bullet O_2^-$ were the active species for this reaction. The nanocomposite displayed good reusability for up to five cycles, with an efficiency of >89%[67]. A novel TiO_2@HKUST-1 nanoreactor was prepared, as shown in Figure 8a. SEM images of HKUST-1 showed an octahedral form, while for the TiO_2@HKUST-1 nanoreactor, a yolk–shell morphology with a decrease in particle size of HKUST-1 was observed. TEM and HRTEM images of the TiO_2@HKUST-1 confirmed the formation of the shell with HKUST-1 (Figure 8b). HRTEM images revealed lattice stripes of 0.346 nm and 0.543 nm, corresponding to the (511) plane of HKUST-1 and the (101) plane of anatase TiO_2, respectively (Figure 8c). TiO_2@HKUST-1 showed better photocatalytic performance than bare materials. It could degrade RhB and TC with an efficiency of 95.2% and 92.40% in 60 min under visible light radiation. The suggested mechanism is shown in Figure 8d. ESR and density function theory (DFT) calculations indicated h^+ and •OH as the main active species. The photocatalytic performance of composite material reached 89.0 % after five cycles [105].

Cen et al. developed ZIF-8/TiO_2 nanofibers comprised of TiO_2 nanoparticles and ZIF-8, as illustrated in Figure 9a. SEM images showed that ZIF-8/TiO_2 nanofibers contained plenty of nanoparticles on the surface and within the nanofibers (Figure 9b,c). The ZIF-8/TiO_2 NFs-10 degraded 95.4% of RhB molecules under UV light irradiation in 240 min. Its photodegradation mechanism is illustrated in Figure 9d. According to trapping experiments, •OH was identified as the primary reactive species, aided by $\bullet O_2^-$ and h^+ [25].

Bismuth oxide (Bi_2O_3) is a visible light-activated photocatalyst with a short bandgap and high oxidizing ability. Sharma et al. prepared Bi_2O_3@Fe-SA composite materials using Bi_2O_3 and Fe-SA (iron succinic acid organic frameworks) by a hydrothermal approach. The bandgaps of Bi_2O_3, Fe-SA, and Bi_2O_3@Fe-SA (1) were calculated to be 2.99 eV, 1.66 eV, and 1.55 eV, respectively. Bi_2O_3@Fe-SA (1) (molar ratios of Fe: Bi = 1:0.1) revealed the highest efficiency of 80% for the decomposition of RhB within 120 min under visible light. Trapping experiments indicated •OH as the main species in this reaction. Bi_2O_3@Fe-SA (1) maintained its efficiency after four catalytic cycles [80]. $BaTiO_3$@ZIF-8 (Z/BTO) nanocomposites were synthesized by growing ZIF-8 on the $BaTiO_3$ surface. The Z/BTO-25 (with a 25% loading ratio of BTO NPs) had a bandgap of 3.1 eV. $BaTiO_3$@ZIF-8-25 degraded

93% of MB in 180 min and 100% of CR in 75 min under solar light. Trapping experiments revealed that the superoxide anion radicals and hydroxyl radicals are the important species in the photocatalytic reaction. The composite material exhibited good cyclability and maintained its performance over four cycles [24]. Hekmat et al. synthesized bismuth vanadate ($BiVO_4$) using a hydrothermal method with 1-ethyl-3-methylimidazolium ethyl sulfate [Emim][$EtSO_4$] ionic liquids (IL-2). The photocatalytic efficiency of $BiVO_4$ was enhanced by growing MIL-100(Fe) on its surface to form $BiVO_4$-MIL-100(Fe) composite material. Figure 10a shows the synthesis scheme of IL-$BiVO_4$-MIL-100(Fe) composite material. It showed a reduced recombination rate, according to PL spectra. The composite material outperformed bare $BiVO_4$, degrading 90% of Basic Red 46 (BR46) in 120 min under visible light. The mechanism of photocatalytic reaction with composite material is inserted in Figure 10b. Scavenger experiments indicated that $\bullet O_2^-$ and holes were crucial in the photocatalytic process [79].

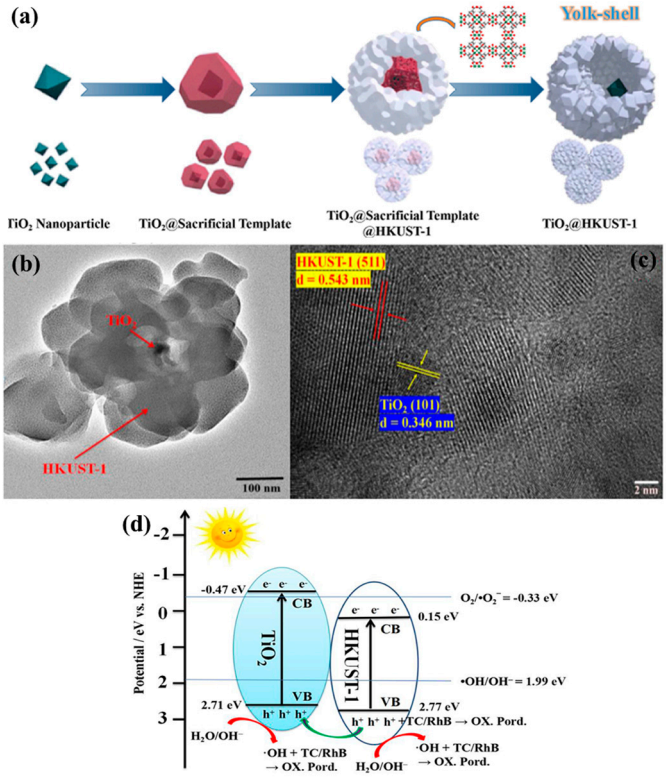

Figure 8. (**a**) Synthesis illustration of TiO_2@HKUST-1; (**b**) TEM image and (**c**) HRTEM image of TiO_2@HKUST-1; and (**d**) photocatalytic mechanism of TiO_2@HKUST-1. Adapted with permission from [105]. Copyright 2023 Elsevier.

Ag_3PO_4@ZIF-8 composite materials were synthesized using ZIF-8 and silver phosphate. The bandgaps of ZIF-8, Ag_3PO_4, and Ag_3PO_4@ZIF-8 were calculated as 5.25 eV, 2.38 eV, and 2.15 eV, respectively. The total organic carbon (TOC) results showed that Ag_3PO_4@ZIF-8-5% could degrade 99.0% of RhB, 90.7% of Crystal Violet (CV), and 94.7% of CR within 120 min under visible light. Its excellent photocatalytic performance was due to extended light absorption and suppressed charge recombination. Superoxide anion radicals, hydroxyl radicals, and holes were key factors in the photocatalytic reaction. The composite material showed excellent stability over five cycles [66]. Silver tungstate (Ag_2WO_4) is known for its great photocatalytic performance and conductivity. Ag_2WO_4-supported ZIF-8 hybrid materials were constructed via the hydrothermal method. The bandgaps for ZIF-8, Ag_2WO_4, and Ag_2WO_4/ZIF-8 were 4.6 eV, 3.06 eV, and 1.8 eV, respectively. Ag_2WO_4/ZIF-8 efficiently degraded 98.3% of MB upon exposed to visible light within 120 min. The enhanced activity was related to efficient charge separation and the

presence of plasmonic Ag. Trapping experiments identified $\bullet O_2^-$ as the primary reactive species. The composite material demonstrated excellent photostability over five cycles, as confirmed by XRD and FESEM analysis [106]. Wu et al. synthesized $AgVO_3$@ ZIF(Zn, Co) composite materials with bimetallic ZIF(Zn, Co) and silver vanadate ($AgVO_3$) under hydrothermal reaction. The bandgaps of ZIF (Zn, Co), $AgVO_3$, and $AgVO_3$@ZIF(Zn, Co) were calculated as 3.67 eV, 2.13 eV, and 1.38 eV, respectively. ESR results confirmed that •OH and $\bullet O_2^-$ are critical for the photocatalytic reactions. The photocatalytic efficiency of the composite material decreased to 82.2% after five cycles [107]. ZIF-8/Ag_2CO_3/CF (cotton fabrics) photocatalyst was synthesized using the SILAR method (Figure 11a). The bandgaps for ZIF-8/CF, Ag_2CO_3/CF, and ZIF-8/Ag_2CO_3/CF-10 (the SILAR method was repeated 10 times) were 3.07, 2.46, and 1.93 eV, respectively. According to Figure 11b, HRTEM images showed Ag_2CO_3 was uniformly distributed on ZIF-8 nanoparticles. ZIF-8/Ag_2CO_3/CF-10 achieved 91% efficiency toward RhB removal in 30 min, which was 15-fold higher than the photocatalytic activity of ZIF-8/CF. The putative mechanism for photocatalytic elimination of RhB with ZIF-8/Ag_2CO_3/CF is shown in Figure 11c. Scavenger experiments identified h^+ as the main active species, followed by $\bullet O_2^-$ and •OH [108].

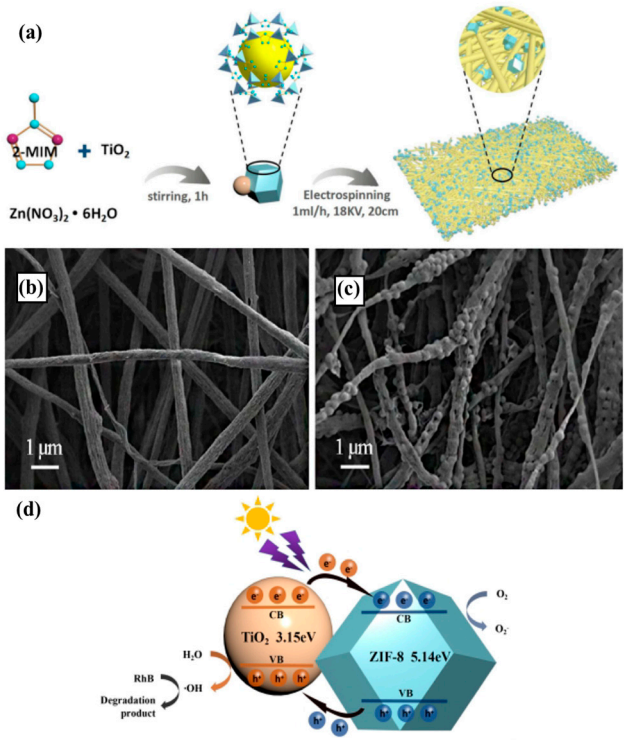

Figure 9. (**a**) Synthesis illustration of ZIF-8/TiO_2 NFs; (**b**) SEM images of PVDF NFs and (**c**) ZIF-8/TiO_2 NFs-10; and (**d**) mechanism of photocatalytic reaction of the composite material for degradation of RhB. Adapted with permission from [25]. Copyright 2023 Elsevier.

BiOBr-based photocatalysts have received considerable interest in wastewater remediation. However, the practical application of bare BiOBr is limited by charge carrier recombination. MIL-125(Ti)-NH_2 (Ti-MOF) was synthesized with a solvothermal procedure and used to synthesize BiOBr/MIL-125(Ti)-NH_2 (BTN) composite materials with BiOBr. The bandgaps of BiOBr, MIL-125(Ti)-NH_2, and BTN-4 (mass ratio of MOF = 60%) were reported to be 2.98, 2.66, and 2.68 eV, respectively. The optimal composite (BTN-4) showed the best activity for the degradation of MO, with an efficiency of 91% in 180 min of exposure to visible light. The generation of heterojunction structures facilitates charge carrier transfer and improves the photocatalytic efficiency of the composite material. Scavenger tests and ESR proved that h^+ and $\bullet O_2^-$ play important roles in MO elimination, while •OH has a slight effect. BTN-4 showed good stability, and its performance decreased to

84% after four cycles [109]. For more details, the photocatalytic efficiencies of some of MOF–semiconductor composite materials are listed in Table 4.

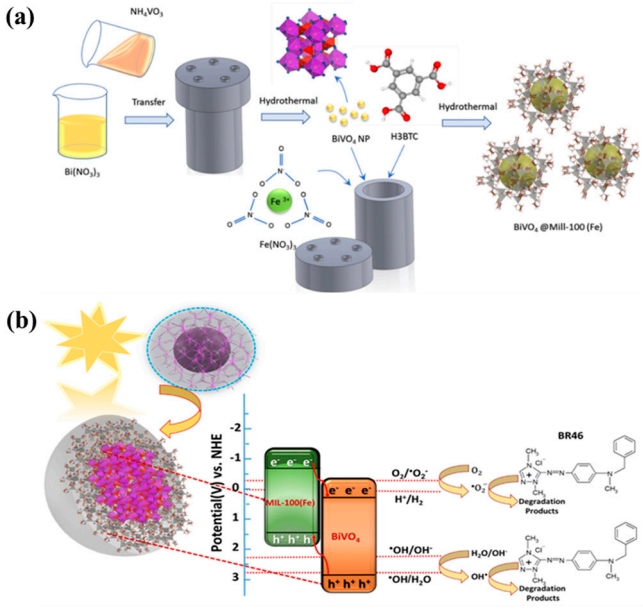

Figure 10. (**a**) Synthesis scheme of IL-$BiVO_4$-MIL-100(Fe) through a hydrothermal process; and (**b**) schematic of the photo-induced electron–hole pair transfer process of IL2-$BiVO_4$-MIL-100(Fe) under visible light. Adapted with permission from [79]. Copyright 2023 Elsevier.

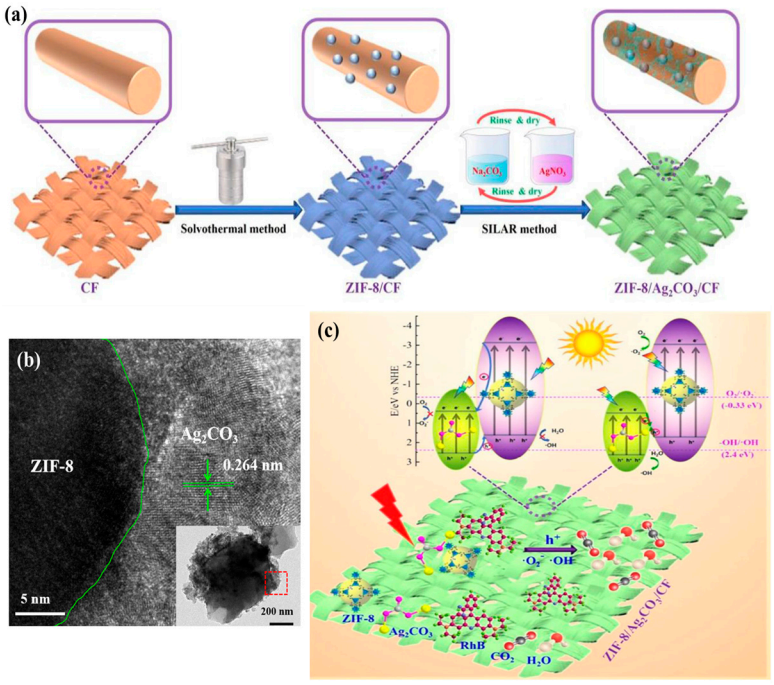

Figure 11. (**a**) Fabrication of photocatalytic cotton fabrics functionalized with ZIF-8/Ag_2CO_3 composite material; (**b**) HRTEM images of ZIF-8/Ag_2CO_3 /CF-10; and (**c**) proposed photocatalytic mechanism of ZIF-8/Ag_2CO_3/CF for dye degradation. Adapted with permission from [108]. Copyright 2023 Elsevier.

Table 4. Comparison of the photocatalytic efficiencies of some MOF–semiconductor composite materials towards dyes.

Catalyst	Light Source	Dye	Dye Conc. (mg L^{-1})	Catalyst Dosage (mg mL^{-1})	Reaction Time (min)	Degradation (%)	Ref.
ZIF-8/TiO_2NFs-10	UV	RhB	10	0.2	240	95.4	[25]
BiVO4-MIL-100(Fe)	Vis	Basic Red 46	10	0.5	120	90	[79]
Bi_2O_3@Fe-SA	Vis	RhB	10	0.1	120	80	[80]
MoS_2-HKUST-1	Vis	RhB	50	0.25	30	96.4	[81]
CdS/Mn-MOF (50)	Vis	RhB	10	0.15	60	98.7	[82]
$BaTiO_3$@ZIF-8-25	Solar	MB CR	10 25	-	180 75	93 100	[24]
ZnO@HKUST-1	Sunlight	RB	20	0.32	45	97.4	[67]
TiO_2@HKUST-1	Vis	RhB	0.002 mmol L^{-1}	0.3	60	95.2	[105]
Ag_3PO_4@ZIF-8-5%	Vis	CV CR	20 20	0.4 0.4	120 120	90.7 94.7	[66]
Ag_2WO_4@ZIF-8	Vis	MB	30	0.1	120	98.3	[106]
$AgVO_3$@BZIF-3	Vis	MB	20	1	180	98.2	[107]
ZIF-8/Ag_2CO_3/CF-10	Sunlight	RhB	10	-	30	91	[108]
BiOBr/MIL-125-(NH_2)	Vis	MO	20	1	180	91	[109]

Roy et al. designed MS-HK nanocomposite materials using Cu-MOF (HKUST-1; HK) and MoS_2 nanosheets (MS). The bandgap data of MoS_2, HKUST-1, and MS-HK were found to be 2.14 eV, 3.07 eV, and 1.44 eV, respectively. The MS-HK photocatalyst degraded 96.4% of RB within 30 min under visible light irradiation. The enhanced photocatalytic activity of the composite material was due to the combination of HKUST-1 with MoS_2, leading to a short bandgap, which resulted in enhanced visible light absorption and the efficient separation and transport of electrons and holes. Radical trapping experiments revealed that •OH and $\bullet O_2^-$ play critical roles in the photodegradation of RB with MS-HK. The MS-HK nanocomposite displayed significant stability with efficiency of >89% for up to four successive cycles [81]. Cadmium sulfide (CdS) is a notable focus in photocatalysis research because of its ideal bandgap for visible light utilization and strong reduction capability. However, its photocatalytic efficiency is limited by rapid carrier recombination and significant photo-corrosion. To address these issues, CdS is often used as a reducing photocatalyst in developing new heterojunctions to overcome the above drawbacks [110]. Zhu et al. proposed a strategy of combining CdS with MOFs to address the issue of agglomeration of CdS nanoparticles. They synthesized 3D Mn-MOF under solvothermal reaction using the ligand H_2L (H_2L = 5-(pyrazin-2-yl) isophthalic acid). Mn-MOF was used for the synthesis of CdS/Mn-MOF composite materials. The bandgaps of CdS, Mn-MOF, and CdS/Mn-MOF (50) were reported as 2.08 eV, 2.73 eV, and 2.16 eV, respectively. CdS/Mn-MOF (50) (weight ratio of CdS was 49.9% by ICP) degraded 98.7% of RhB within 60 min of exposure to visible light, which was 19.7- and 2.3-fold better than that of Mn-MOF and CdS, respectively. Formation of a heterojunction limited the electron–hole recombination in the composite material. Scavenger tests and ESR analysis indicated $\bullet O_2^-$ as the important active species for this reaction [82].

5. Conclusions and Future Perspective

Metal–organic frameworks (MOFs) have recently demonstrated potential applications in the adsorption and elimination of hazardous contaminants in wastewater. As crystalline porous materials with a high surface area and unique structure flexibility, MOFs are good candidates for wastewater remediation. However, some MOFs suffer from low photocatalytic efficiency and poor water stability. Various approaches, including ligand functionalization, metal nanoparticle doping, surface modification, immobilization of functionalized materials, and fabrication of composite materials, have been adopted to form multifunctional materials.

The development of MOF-based composite materials has recently made prominent progress, introducing new capabilities in material engineering and environmental sustainability. This review summarizes the synthesis and application of novel MOF-based composite materials to eliminate contaminants in wastewater under photocatalytic pro-

cesses. Many of the studies, especially those summarized in this review, use dyes as model contaminants because of the ability to monitor their breakdown using conventional spectroscopic methods. A literature survey revealed that the design and development of MOF-based composite materials resulted in tunable bandgaps, efficient visible light absorption, reduced recombination between photogenerated species, enhanced water stability, better regeneration, and appropriate supramolecular interactions, which significantly enhanced the efficient and selective decomposition of organic dye contaminants.

Despite noteworthy progress, the transition from laboratory research to industrial performance remains challenging because of cost, energy consumption, and environmental impact. The preparation of some MOFs involves costly metal ions or linkers, which can hinder their economic feasibility for widespread applications. Solvothermal methods, commonly used for synthesizing MOFs and their composite materials, are typically unavailable for industrial large-scale applications. The development of solvent-free methods, or nontoxic solvents for the synthesis of these materials on a large scale is necessary. Furthermore, metal ions and organic linkers affect the toxicity of MOFs. For example, the leaching of metal ions like cadmium from MOFs can cause environmental health risks. Also, the photocatalytic reactions for eliminating organic dyes with MOF-based composites may produce byproducts that could be toxic or harmful. Hence, further research is essential to identify, characterize, and evaluate the toxicity of the byproducts of MOF-catalyzed reactions. Understanding these aspects will improve the design of MOF-based photocatalysts and ensure that their use in wastewater remediation is environmentally friendly and sustainable.

Author Contributions: F.M.: Conceptualization, Validation, Writing—original draft. L.G.B.: Conceptualization, Validation, Writing—review and editing. All authors have read and agreed to the published version of the manuscript.

Funding: This research received no external funding.

Acknowledgments: This work was supported by the University of Miami.

Conflicts of Interest: The authors declare that they have no conflicts of interest.

References

1. Khan, M.S.; Li, Y.; Li, D.S.; Qiu, J.; Xu, X.; Yang, H.Y. A review of metal-organic framework (MOF) materials as an effective photocatalyst for degradation of organic pollutants. *Nanoscale Adv.* **2023**, *2*, 6318–6348. [CrossRef] [PubMed]
2. Garg, R.; Sabouni, R.; Alaamer, A.; Alali, A.; Al-Muqbel, D.; Alqassem, H.; Almazrooei, K. Recent development in metal-organic framework-based hybrid nanocomposites for pollutants remediation from wastewater: Challenges and opportunities. *Environ. Technol. Innov.* **2023**, *32*, 103446. [CrossRef]
3. Amenaghawon, A.N.; Anyalewechi, C.L.; Osazuwa, O.U.; Elimian, E.A.; Eshiemogie, S.O.; Oyefolu, P.K.; Kusuma, H.S. A comprehensive review of recent advances in the synthesis and application of metal-organic frameworks (MOFs) for the adsorptive sequestration of pollutants from wastewater. *Sep. Purif. Technol.* **2023**, *311*, 123246. [CrossRef]
4. Oladoye, P.O.; Kadhom, M.; Khan, I.; Hama Aziz, K.H.; Alli, Y.A. Advancements in adsorption and photodegradation technologies for Rhodamine B dye wastewater treatment: Fundamentals, applications, and future directions. *Green Chem. Eng.* **2024**, *5*, 440–460. [CrossRef]
5. Mahmoudi, F.; Saravanakumar, K.; Maheskumar, V.; Njaramba, L.K.; Yoon, Y.; Park, C.M. Application of perovskite oxides and their composites for degrading organic pollutants from wastewater using advanced oxidation processes: Review of the recent progress. *J. Hazard. Mater.* **2022**, *436*, 129074. [CrossRef]
6. Samarasinghe, L.V.; Muthukumaran, S.; Baskaran, K. Recent advances in visible light-activated photocatalysts for degradation of dyes: A comprehensive review. *Chemosphere* **2024**, *349*, 140818. [CrossRef] [PubMed]
7. Aramesh, N.; Reza Bagheri, A.; Zhang, Z.; Yadollahi, B.; Kee Lee, H. Polyoxometalate-based materials against environmental pollutants: A review. *Coord. Chem. Rev.* **2024**, *507*, 215767. [CrossRef]
8. Solayman, H.M.; Abd Aziz, A.; Yahya, N.Y.; Leong, K.H.; Sim, L.C.; Hossain, M.K.; Khan, M.B.; Zoh, K.D. CQDs embed g-C_3N_4 photocatalyst in dye removal and hydrogen evolution: An insight review. *J. Water Process Eng.* **2024**, *57*, 104645. [CrossRef]
9. Mathew, S.; Ramachandra, M.; Devi, K.R.S.; Pinheiro, D.; Manickam, S.; Peng, C.H.; Sonawane, S.H. Synthesis, mechanisms, challenges, and future prospects of Ti_3C_2 MXene and its heterojunctions for photocatalytic dye degradation efficiency: A comprehensive review. *Mater. Today Sustain.* **2023**, *24*, 100568. [CrossRef]

10. Zhao, J.; Guo, T.; Wang, H.; Yan, M.; Qi, Y. BiOBr nanoflakes with engineered thickness for boosted photodegradation of RhB under visible light irradiation. *J. Alloys Compd.* **2023**, *947*, 169613. [CrossRef]
11. Chabalala, M.B.; Mothudi, B.M.; Ntsendwana, B. MOF based nanocomposites for photocatalytic degradation of pollutants in water: A critical review. *J. Photochem. Photobiol. A Chem.* **2024**, *447*, 115244. [CrossRef]
12. Sarker, T.; Tahmid, I.; Sarker, R.K.; Dey, S.C.; Islam, M.T.; Sarker, M. ZIF-67-based materials as adsorbent for liquid phase adsorption-a review. *Polyhedron* **2024**, *260*, 117069. [CrossRef]
13. Tang, S.; Wang, Y.; He, P.; Wang, Y.; Wei, G. Recent Advances in Metal-Organic Framework (MOF)-Based Composites for Organic Effluent Remediation. *Materials* **2024**, *17*, 2660. [CrossRef] [PubMed]
14. Alvaro, M.; Carbonell, E.; Ferrer, B.; Llabrés I Xamena, F.X.; Garcia, H. Semiconductor behavior of a metal-organic framework (MOF). *Chem. Eur. J.* **2007**, *13*, 5106–5112. [CrossRef]
15. Chen, D.; Zheng, Y.T.; Huang, N.Y.; Xu, Q. Metal-organic framework composites for photocatalysis. *Energy Chem.* **2023**, *6*, 100115. [CrossRef]
16. Wen, Y.; Zhang, P.; Sharma, V.K.; Ma, X.; Zhou, H.C. Metal-organic frameworks for environmental applications. *Cell. Rep. Phys. Sci.* **2021**, *2*, 100342. [CrossRef]
17. Rabiee, N. Sustainable metal-organic frameworks (MOFs) for drug delivery systems. *Mater. Today Commun.* **2023**, *35*, 106244. [CrossRef]
18. Yuvaraj, A.R.; Jayarama, A.; Sharma, D.; Nagarkar, S.S.; Duttagupta, S.P.; Pinto, R. Role of metal-organic framework in hydrogen gas storage: A critical review. *Int. J. Hydrogen Energy* **2024**, *59*, 1434–1458. [CrossRef]
19. Shahzad, U.; Marwani, H.M.; Saeed, M.; Asiri, A.M.; Althomali, R.H.; Rahman, M.M. Exploration of porous metal-organic frameworks (MOFs) for an efficient energy storage application. *J. Energy Storage* **2023**, *74*, 109518. [CrossRef]
20. He, Y.; Liu, W.; Liu, J. MOF-based/derived catalysts for electrochemical overall water splitting. *J Colloid Interface Sci.* **2024**, *661*, 409–435. [CrossRef]
21. Zha, F.; Shi, M.; Li, H.; Rao, J.; Chen, B. Biomimetic mineralization of lipase@MOF biocatalyst for ease of biodiesel synthesis: Structural insights into the catalytic behavior. *Fuel* **2024**, *357*, 129854. [CrossRef]
22. Zhang, Y.; Yu, X.; Hou, Y.; Liu, C.; Xie, G.; Chen, X. Current research status of MOF materials for catalysis applications. *Mol. Catal.* **2024**, *555*, 113851. [CrossRef]
23. Wang, Z.; Yue, X.; Xiang, Q. MOFs-based S-scheme heterojunction photocatalysts. *Coord. Chem. Rev.* **2024**, *504*, 215674. [CrossRef]
24. Swain, J.; Priyadarshini, A.; Hajra, S.; Panda, S.; Panda, J.; Samantaray, R.; Yamauchi, Y.; Han, M.; Kim, H.J.; Sahu, R. Photocatalytic dye degradation by $BaTiO_3$/zeolitic imidazolate framework composite. *J. Alloys Compd.* **2023**, *965*, 171438. [CrossRef]
25. Cen, L.; Tang, T.; Yu, F.; Wu, H.; Li, C.; Zhu, H.; Guo, Y. Fabrication of ZIF-8/TiO_2 electrospinning nanofibers for synergistic photodegradation in dyeing wastewater. *J. Ind. Eng. Chem.* **2023**, *126*, 537–545. [CrossRef]
26. Chen, P.; Zhang, H.; Miao, Y.; Tian, C.; Li, W.; Song, Y.; Zhang, Y. Influence of the Conductivity of Polymer Matrix on the Photocatalytic Activity of PAN–PANI–ZIF8 Electrospun Fiber Membranes. *Fibers Polym.* **2023**, *24*, 1253–1264. [CrossRef]
27. Shahriyari Far, H.; Najafi, M.; Hasanzadeh, M.; Rahimi, R. Synthesis of MXene/Metal-Organic Framework (MXOF) composite as an efficient photocatalyst for dye contaminant degradation. *Inorg. Chem. Commun.* **2023**, *152*, 110680. [CrossRef]
28. Bouider, B.; Haffad, S.; Bouakaz, B.S.; Berd, M.; Ouhnia, S.; Habi, A. MOF-5/Graphene Oxide Composite Photocatalyst for Enhanced Photocatalytic Activity of Methylene Blue Degradation Under Solar Light. *J. Inorg. Organomet. Polym. Mater.* **2023**, *33*, 4001–4011. [CrossRef]
29. Li, L.Y.; Wang, X.; Ma, L.X.; Zhou, W.J.; Li, B.L.; Li, H.Y.; Hu, C.J. A two-dimensional Cu(II) metal-organic framework and its g-C_3N_4 heterojunction composite for high efficient photodegradation of organic dyes. *J. Solid State Chem.* **2023**, *326*, 124173. [CrossRef]
30. Li, L.; Han, J.; Huang, X.; Qiu, S.; Liu, X.; Liu, L.; Zhao, M.; Qu, J.; Zou, J.; Zhang, J. Organic pollutants removal from aqueous solutions using metal-organic frameworks (MOFs) as adsorbents: A review. *J. Environ. Chem. Eng.* **2023**, *11*, 111217. [CrossRef]
31. Bhuyan, A.; Ahmaruzzaman, M. Recent advances in MOF-5-based photocatalysts for efficient degradation of toxic organic dyes in aqueous medium. *Next Sustain.* **2024**, *3*, 100016. [CrossRef]
32. Sağlam, S.; Türk, F.N.; Arslanoğlu, H. Use and applications of metal-organic frameworks (MOF) in dye adsorption: Review. *J. Environ. Chem. Eng.* **2023**, *11*, 110568. [CrossRef]
33. Zhao, H.; Xing, Z.; Su, S.; Song, S.; Xu, T.; Li, Z.; Zhou, W. Recent advances in metal organic frame photocatalysts for environment and energy applications. *Appl. Mater. Today* **2020**, *21*, 100821. [CrossRef]
34. Sandhu, Z.A.; Farwa, U.; Danish, M.; Raza, M.A.; Talib, A.; Amjad, H.; Riaz, R.; Al-Sehemi, A.G. Sustainability and photocatalytic performance of MOFs: Synthesis strategies and structural insights. *J. Clean. Prod.* **2024**, *470*, 143263. [CrossRef]
35. Singh, V.; Gautam, S.; Kaur, S.; Kajal, N.; Kaur, M.; Gupta, R. Highly functionalized photo-activated metal–organic frameworks for dye degradation: Recent advancements. *Mater. Today Commun.* **2023**, *34*, 105180. [CrossRef]
36. Juma, A.K.; Merican, Z.M.A.; Haruna, A. Recent progress of MOF-based photocatalysts for environmental application and sustainability considerations. *Chem. Eng. Res. Des.* **2024**, *208*, 391–435. [CrossRef]
37. Nasalevich, M.A.; Goesten, M.G.; Savenije, T.J.; Kapteijn, F.; Gascon, J. Enhancing optical absorption of metal-organic frameworks for improved visible light photocatalysis. *Chem. Comm.* **2013**, *49*, 10575–10577. [CrossRef]

38. Naghdi, S.; Shahrestani, M.M.; Zendehbad, M.; Djahaniani, H.; Kazemian, H.; Eder, D. Recent advances in application of metal-organic frameworks (MOFs) as adsorbent and catalyst in removal of persistent organic pollutants (POPs). *J. Hazard. Mater.* **2023**, *442*, 130127. [CrossRef]
39. Kaur, B.; Soni, V.; Kumar, R.; Singh, P.; Selvasembian, R.; Singh, A.; Thakur, S.; Parwaz Khan, A.A.; Kaya, S.; Nguyen, L.H.; et al. Recent advances in manipulating strategies of NH_2-functionalized metallic organic frameworks-based heterojunction photocatalysts for the sustainable mitigation of various pollutants. *Environ. Res.* **2024**, *259*, 119575. [CrossRef]
40. Liaqat, R.; Jamshaid, M.; Abo-Dief, H.M.; Ali, S.E.; El-Bahy, Z.M.; Fiaz, M.; Wattoo, M.A.; Rehman, A.u. Mo@Ni-MOF nanocomposite: A promising photocatalyst for photodegradation of Methylene blue. *J. Mol. Struct.* **2024**, *1315*, 139011. [CrossRef]
41. Redwan Habib, N.; Taddesse, A.M.; Sainz, R.; Sánchez-Sánchez, M.; Diaz, I. Copper-loaded sustainable MOFs as photocatalysts for dye removal. *J. Photochem. Photobiol. A Chem.* **2024**, *456*, 115842. [CrossRef]
42. Zhang, L.L.; Liu, M.; Wang, K.A.; Bin Zhu, H. Assembling Ag/UiO-66-NH_2 Composites for Photocatalytic Dye Degradation. *J. Inorg. Organomet. Polym. Mater.* **2022**, *32*, 1896–1901. [CrossRef]
43. Pan, Y.; Abazari, R.; Tahir, B.; Sanati, S.; Zheng, Y.; Tahir, M.; Gao, J. Iron-based metal–organic frameworks and their derived materials for photocatalytic and photoelectrocatalytic reactions. *Coord. Chem. Rev.* **2024**, *499*, 215538. [CrossRef]
44. Zhao, N.; Sun, F.; Zhang, N.; Zhu, G. Novel Pyrene-Based Anionic Metal-Organic Framework for Efficient Organic Dye Elimination. *Cryst. Growth Des.* **2017**, *17*, 2453–2457. [CrossRef]
45. Li, S.; Yang, S.; Liang, G.; Yan, M.; Wei, C.; Lu, Y. Regulation and photocatalytic degradation mechanism of a hydroxyl modified UiO-66 type metal organic framework. *RSC Adv.* **2023**, *13*, 5273–5282. [CrossRef]
46. Jing, H.P.; Wang, C.C.; Zhang, Y.W.; Wang, P.; Li, R. Photocatalytic degradation of methylene blue in ZIF-8. *RSC Adv.* **2014**, *4*, 54454–54462. [CrossRef]
47. Yang, S.; Li, X.; Zeng, G.; Cheng, M.; Huang, D.; Liu, Y.; Zhou, C.; Xiong, W.; Yang, Y.; Wang, W.; et al. Materials Institute Lavoisier (MIL) based materials for photocatalytic applications. *Coord. Chem. Rev.* **2021**, *438*, 213874. [CrossRef]
48. Ai, L.; Zhang, C.; Li, L.; Jiang, J. Iron terephthalate metal-organic framework: Revealing the effective activation of hydrogen peroxide for the degradation of organic dye under visible light irradiation. *Appl. Catal. B Environ.* **2014**, *148–149*, 191–200. [CrossRef]
49. Rezaei, H.; Zinatizadeh, A.A.; Joshaghani, M.; Zinadini, S. Amino acid-based carbon quantum dot modified MIL-53 (Fe): Investigation of its visible-driven photocatalytic activity provided by a highly efficient photoreactor. *Mater. Sci. Semicond. Process.* **2023**, *154*, 107190. [CrossRef]
50. Chu, H.; Wang, C.C. MIL-100(Fe)-based functional materials for water decontamination: A state of the art review. *Prog. Nat. Sci.-Mater. Int.* **2023**, *33*, 386–406. [CrossRef]
51. Mahmoodi, N.M.; Abdi, J.; Oveisi, M.; Alinia Asli, M.; Vossoughi, M. Metal-organic framework (MIL-100 (Fe)): Synthesis, detailed photocatalytic dye degradation ability in colored textile wastewater and recycling. *Mater. Res. Bull.* **2018**, *100*, 357–366. [CrossRef]
52. Guesh, K.; Caiuby, C.A.D.; Mayoral, Á.; Díaz-García, M.; Díaz, I.; Sanchez-Sanchez, M. Sustainable Preparation of MIL-100(Fe) and Its Photocatalytic Behavior in the Degradation of Methyl Orange in Water. *Cryst. Growth Des.* **2017**, *17*, 1806–1813. [CrossRef]
53. Xia, L.; Ni, J.; Wu, P.; Ma, J.; Bao, L.; Shi, Y.; Wang, J. Photoactive metal-organic framework as a bifunctional material for 4-hydroxy-4′-nitrobiphenyl detection and photodegradation of methylene blue. *Dalton Trans.* **2018**, *47*, 16551–16557. [CrossRef]
54. Li, H.; Li, Q.; He, X.; Xu, Z.; Wang, Y.; Jia, L. Synthesis of AgBr@MOFs nanocomposite and its photocatalytic activity for dye degradation. *Polyhedron* **2019**, *165*, 31–37. [CrossRef]
55. Gholizadeh Khasevani, S.; Gholami, M.R. Evaluation of the reaction mechanism for photocatalytic degradation of organic pollutants with MIL-88A/BiOI structure under visible light irradiation. *Res. Chem. Intermed.* **2019**, *45*, 1341–1356. [CrossRef]
56. Abdi, J.; Banisharif, F.; Khataee, A. Amine-functionalized Zr-MOF/CNTs nanocomposite as an efficient and reusable photocatalyst for removing organic contaminants. *J. Mol. Liq.* **2021**, *334*, 116129. [CrossRef]
57. Ao, D.; Zhang, J.; Liu, H. Visible-light-driven photocatalytic degradation of pollutants over Cu-doped NH2-MIL-125(Ti). *J. Photochem. Photobiol. A* **2018**, *364*, 524–533. [CrossRef]
58. Faaizatunnisa, N.; Ediati, R.; Yusof, E.N.M.; Fadlan, A.; Karelius, K.; Kulsum, U.; Ariesta, M.N. The mixed-ligand strategy for structural modification of MOF materials to enhance the photocatalytic degradation and adsorption of organic pollutants: A review. *Nano-Struct. Nano-Objects* **2024**, *40*, 101366. [CrossRef]
59. Jin, J.C.; Yang, M.; Zhang, Y.L.; Dutta, A.; Xie, C.G.; Kumar, A. Integration of mixed ligand into a multivariate metal-organic framework for enhanced UV-light photocatalytic degradation of Rhodamine B. *J. Taiwan Inst. Chem. Eng.* **2021**, *129*, 410–417. [CrossRef]
60. Thambiliyagodage, C. Activity enhanced TiO_2 nanomaterials for photodegradation of dyes—A review. *Environ. Nanotechnol. Monit. Manag.* **2021**, *16*, 100592. [CrossRef]
61. Duran, F.; Diaz-Uribe, C.; Vallejo, W.; Muñoz-Acevedo, A.; Schott, E.; Zarate, X. Adsorption and Photocatalytic Degradation of Methylene Blue on TiO_2 Thin Films Impregnated with Anderson-Evans Al-Polyoxometalates: Experimental and DFT Study. *ACS Omega* **2023**, *8*, 27284–27292. [CrossRef] [PubMed]
62. Che Ramli, Z.A.; Asim, N.; Isahak, W.N.R.W.; Emdadi, Z.; Ahmad-Ludin, N.; Yarmo, M.A.; Sopian, K. Photocatalytic degradation of methylene blue under UV light irradiation on prepared carbonaceous TiO_2. *Sci. World J.* **2014**, *2014*, 415136. [CrossRef] [PubMed]
63. Ramanathan, G.; Murali, K.R. Photocatalytic activity of SnO_2 nanoparticles. *J. Appl. Electrochem.* **2022**, *52*, 849–859. [CrossRef]

64. Dharmana, G.; Nadikatla, S.K.; Gurugubelli, T.R.; Viswanadham, B. Enhanced Photo-Catalytic Degradation of MB Dye over Hydrothermal Grown-Up of ZnO/SnO_2 Catalyst. *J. Chem.* **2024**, *2024*, 9135923. [CrossRef]
65. Roy, S.; Darabdhara, J.; Ahmaruzzaman, M. Recent advances of Copper-BTC metal-organic frameworks for efficient degradation of organic dye-polluted wastewater: Synthesis, mechanistic insights and future outlook. *J. Hazard. Mater. Lett.* **2024**, *5*, 100094. [CrossRef]
66. Motora, K.G.; Wu, C.M.; Lin, S.-T. Novel Ag_3PO_4@ZIF-8 p-n heterojunction for effective photodegradation of organic pollutants. *J. Water Process Eng.* **2023**, *52*, 103586. [CrossRef]
67. Roy, S.; Darabdhara, J.; Ahmaruzzaman, M. ZnO-based Cu metal–organic framework (MOF) nanocomposite for boosting and tuning the photocatalytic degradation performance. *Environ. Sci. Pollut. Res.* **2023**, *30*, 95673–95691. [CrossRef]
68. Xue, Y.; Zheng, S.; Xue, H.; Pang, H. Metal-organic framework composites and their electrochemical applications. *J. Mater. Chem. A* **2019**, *7*, 7301–7327. [CrossRef]
69. Chen, J.Q.; Sharifzadeh, Z.; Bigdeli, F.; Gholizadeh, S.; Li, Z.; Hu, M.L.; Morsali, A. MOF composites as high potential materials for hazardous organic contaminants removal in aqueous environments. *J. Environ. Chem. Eng.* **2023**, *11*, 109469. [CrossRef]
70. Naeem, A.; Saeed, T.; Sayed, M.; Ahmad, B.; Mahmood, T.; Farooq, M.; Perveen, F. Chitosan decorated zirconium metal-organic framework for collaborative adsorption and photocatalytic degradation of methylene blue and methyl orange. *Process Saf. Environ. Prot.* **2023**, *176*, 115–130. [CrossRef]
71. Niu, H.Y.; Cao, L.Q.; Yang, X.L.; Liu, K.N.; Liu, L.; Wang, J.D. In situ growth of the ZIF-8 on the polymer monolith via CO_2-in-water HIPEs stabilized using metal oxide nanoparticles and its photocatalytic activity. *Polym. Adv. Technol.* **2021**, *32*, 3194–3204. [CrossRef]
72. Guo, A.; Wang, X.; Liu, H.; Li, X.; Yang, L.; Yang, W. Efficient photocatalytic degradation of water contaminants via Ag decorated porphyrin-based organic framework materials. *Surf. Interfaces* **2023**, *38*, 102843. [CrossRef]
73. Chen, X.H.; Zhang, Y.S.; Li, W.B.; Guan, X.W.; Ye, J.W.; Chen, L.; Wang, H.P.; Bai, J.; Mo, Z.W.; Chen, X.M. A porphyrin-based metal-organic framework with highly efficient adsorption and photocatalytic degradation performances for organic dyes. *Inorg. Chem. Front.* **2022**, *9*, 2328–2335. [CrossRef]
74. Lafta, M.A.; Ammar, S.H. Synthesis and photocatalytic activity of polyoxometalates immobilized onto g-C_3N_4/ZIF-67 heterostructures. *Mater. Sci. Semicond. Process.* **2023**, *153*, 107131. [CrossRef]
75. Zhou, W.-J.; Ma, L.-X.; Li, L.-Y.; Zha, M.; Li, B.-L.; Wu, B.; Hu, C.H. Synthesis of a 3D Cu(II) MOF and its heterostructual g-C3N4 composite showing improved visible-light-driven photodegradation of organic dyes. *J. Solid State Chem.* **2022**, *315*, 123520. [CrossRef]
76. Rahmani, M.; Abbasi, A.; Hosseini, M.S. Fabrication of visible light responsive nitrogen-doped carbon quantum dots/MIL-101(Cr) composites for enhanced photodegradation of Rhodamine B. *J. Photochem. Photobiol. A Chem.* **2023**, *445*, 115019. [CrossRef]
77. El-Fawal, E.M.; Morshedy, A.S. Fabrication of Mn@Zr-MOF composite for highly efficient photocatalytic oxidative desulfurization of liquid fuels and degradation of dyes: Application of response surface methodology. *Inorg. Chem. Commun.* **2024**, *170*, 113272. [CrossRef]
78. Ghasemzadeh, R.; Akhbari, K. Heterostructured Ag@MOF-801/MIL-88A(Fe) Nanocomposite as a Biocompatible Photocatalyst for Degradation of Reactive Black 5 under Visible Light. *Inorg. Chem.* **2023**, *62*, 17818–17829. [CrossRef]
79. Hekmat, A.; Ghasemi, S.; Vossoughi, M. Unveiling the synergistic effect of ionic liquid and metal-organic framework on the efficiency of $BiVO_4$: $BiVO_4$-MIL-100(Fe) as a visible light-induced photocatalyst for Basic Red 46 degradation. *J. Environ. Chem. Eng.* **2023**, *11*, 110658. [CrossRef]
80. Sharma, A.; Kumari, M.; Tahir, M.; Jain, S.; Sharma, S.; Kumar, N. An energy saving and water- based synthesis of Bi_2O_3@Fe-succinate MOF: A visible light mediated approach towards water decontamination. *J. Mol. Liq.* **2023**, *386*, 122429. [CrossRef]
81. Roy, S.; Darabdhara, J.; Ahmaruzzaman, M. MoS_2 Nanosheets@Metal organic framework nanocomposite for enhanced visible light degradation and reduction of hazardous organic contaminants. *J. Clean. Prod.* **2023**, *430*, 139517. [CrossRef]
82. Zhu, C.Y.; Shen, M.T.; Qi, M.J.; Zhao, Y.Y.; Xu, Z.; Li, P.; Ru, J.; Gao, W.; Zhang, X.M. Constructed CdS/Mn-MOF heterostructure for promoting photocatalytic degradation of Rhodamine B. *Dyes Pigm.* **2023**, *219*, 111607. [CrossRef]
83. Oladoye, P.O.; Adegboyega, S.A.; Adebisi Giwa, A.-R. Remediation potentials of composite metal-organic frameworks (MOFs) for dyes as water contaminants: A comprehensive review of recent literatures. *Environ. Nanotechnol. Monit. Manag.* **2021**, *16*, 100568. [CrossRef]
84. Guo, H.; Guo, D.; Zheng, Z.; Weng, W.; Chen, J. Visible-light photocatalytic activity of Ag@MIL-125(Ti) microspheres. *Appl. Organomet. Chem.* **2015**, *29*, 618–623. [CrossRef]
85. Abdi, J. Synthesis of Ag-doped ZIF-8 photocatalyst with excellent performance for dye degradation and antibacterial activity. *Colloids Surf. A Physicochem. Eng. Asp.* **2020**, *645*, 125330. [CrossRef]
86. Chandra, R.; Nath, M. Facile Synthesis of Metal–Organic Framework (ZIF-11) and AgNPs Encapsulated-ZIF-11 Composite as an Effective Heterogeneous Catalyst for Photodegradation of Methylene Blue. *Appl. Organomet. Chem.* **2020**, *34*, e5951. [CrossRef]
87. Zhang, X.; Zhang, S.; Tang, Y.; Huang, X.; Pang, H. Recent advances and challenges of metal–organic framework/ graphene-based composites. *Compos. B Eng.* **2022**, *230*, 109532. [CrossRef]
88. Quang, H.T.; Le Pham, H.A.; Van Cuong, N.; Dang, H.P.; Anh, N.T.H. Rapid Synthesis of Bismuth MOF@Carbon Nanotube Composite by microwave-assisted Solvothermal for Photodegrading RhB. *Top. Catal.* **2024**, *67*, 1155–1168. [CrossRef]

89. Lan, D.; Zhu, H.; Zhang, J.; Xie, C.; Wang, F.; Zheng, Y.; Guo, Z.; Xu, M.; Wu, T. Heterojunction of UiO-66 and porous g-C_3N_4 for boosted photocatalytic removal of organic dye. *Appl. Surf. Sci.* **2024**, *655*, 159623. [CrossRef]
90. Zhang, X.; Song, Z.; Yu, X.; Dong, X.; Peng, Y.; Wei, K.; Cao, L.; He, X.; Zhang, Z.; Fan, J. Construction of heterogeneous structures of MIL-101(Fe)/Ce/g-C_3N_4 nanocomposites for enhanced photocatalytic activity under visible light. *J. Solid State Chem.* **2023**, *323*, 124013. [CrossRef]
91. Durmus, Z.; Köferstein, R.; Lindenberg, T.; Lehmann, F.; Hinderberger, D.; Maijenburg, A.W. Preparation and characterization of Ce-MOF/g-C_3N_4 composites and evaluation of their photocatalytic performance. *Ceram. Int.* **2023**, *49*, 24428–24441. [CrossRef]
92. Mukherjee, D.; Das, P.; Kundu, S.; Mohan Kundu, L.; Mandal, B. Graphene quantum dots decorated MIL-100(Fe) composites for dye degradation. *J. Photochem. Photobiol. A Chem.* **2023**, *442*, 114776. [CrossRef]
93. Yang, H.L.; Bai, L.F.; Geng, Z.R.; Chen, H.; Xu, L.T.; Xie, Y.C.; Wang, D.J.; Gu, H.W.; Wang, X.M. Carbon quantum dots: Preparation, optical properties, and biomedical applications. *Mater. Today Adv.* **2023**, *18*, 100376. [CrossRef]
94. Cheng, L.; Tang, Y.; Xie, M.; Sun, Y.; Liu, H. 2D ultrathin NiMOF decorated by Ti_3C_2 MXene for highly improved photocatalytic performance. *J. Alloys Compd.* **2021**, *864*, 158913. [CrossRef]
95. Shahzaib, A.; Shaily; Kamran, L.A.; Nishat, N. The Biomolecule-MOF Nexus: Recent advancements in biometal-organic frameworks (Bio-MOFs) and their multifaceted applications. *Mater. Today Chem.* **2023**, *34*, 101781. [CrossRef]
96. Zhu, W.; Xia, Z.; Shi, B.; Lü, C. Two-Dimensional Cu-Porphyrin Metal-Organic Framework Nanosheet-Supported Flaky TiO_2 as an Efficient Visible-Light-Driven Photocatalyst for Dye Degradation and Cr(VI) Reduction. *Langmuir* **2023**, *39*, 15665–15675. [CrossRef]
97. Hassanzadeh Goji, N.; Ramezani, M.; Saljooghi, A.S.; Alibolandi, M. Porphyrin-based metal–organic frameworks: Focus on diagnostic and therapeutic applications. *J. Nanostruct. Chem.* **2024**, *14*, 167–208. [CrossRef]
98. Ramasubbu, V.; Ram Kumar, P.; Chellapandi, T.; Madhumitha, G.; Mothi, E.M.; Shajan, X.S. Zn(II) porphyrin sensitized (TiO_2@Cd-MOF) nanocomposite aerogel as novel photocatalyst for the effective degradation of methyl orange (MO) dye. *Opt. Mater.* **2022**, *132*, 112558. [CrossRef]
99. Xiao, L.; Wang, Z.; Guan, J. 2D MOFs and their derivatives for electrocatalytic applications: Recent advances and new challenges. *Coord. Chem. Rev.* **2022**, *472*, 214777. [CrossRef]
100. Wang, Z.; Jing, C.; Zhai, W.; Li, Y.; Liu, W.; Zhang, F.; Li, S.; Wang, H.; Yu, D. MIL-101(Fe)/polysulfone hollow microspheres from pickering emulsion template for effective photocatalytic degradation of methylene blue. *Colloids Surf. A Physicochem. Eng. Asp.* **2023**, *667*, 131394. [CrossRef]
101. Brahmi, C.; Benltifa, M.; Vaulot, C.; Michelin, L.; Dumur, F.; Gkaniatsou, E.; Sicard, C.; Airoudj, A.; Morlet-Savary, F.; Bousselmi, L.; et al. New Hybrid Fe-based MOFs/Polymer Composites for the Photodegradation of Organic Dyes. *Chem. Select.* **2021**, *6*, 8120–8132. [CrossRef]
102. Brahmi, C.; Benltifa, M.; Vaulot, C.; Michelin, L.; Dumur, F.; Millange, F.; Frigoli, M.; Airoudj, A.; Morlet-Savary, F.; Bousselmi, L.; et al. New hybrid MOF/polymer composites for the photodegradation of organic dyes. *Eur. Polym. J.* **2021**, *154*, 110560. [CrossRef]
103. Patial, S.; Sonu; Thakur, S.; Van Le, Q.; Ahamad, T.; Singh, P.; Nguyen, V.H.; Khan, A.A.P.; Hussain, C.M.; Raizada, P. Facile synthesis of Co, Fe-bimetallic MIL-88A/microcrystalline cellulose composites for efficient adsorptive and photo-Fenton degradation of RhB dye. *J. Taiwan Inst. Chem. Eng.* **2023**, *153*, 105189. [CrossRef]
104. Wang, W.; Wen, C.; Zheng, D.; Li, C.; Bian, J.; Wang, X. Simultaneous degradation of RhB and reduction of Cr(VI) by MIL-53(Fe)/Polyaniline (PANI) with the mediation of organic acid. *Chin. J. Chem. Eng.* **2022**, *42*, 55–63. [CrossRef]
105. Qiao, Y.; Sun, C.; Jian, J.; Zhou, T.; Xue, X.; Shi, J.; Che, G.; Liao, G. Efficient removal of organic pollution via photocatalytic degradation over a TiO_2@HKUST-1 yolk-shell nanoreactor. *J. Mol. Liq.* **2023**, *385*, 122383. [CrossRef]
106. Mohammed, R.O.; Amooey, A.A.; Ammar, S.H.; Salman, M.D. Enhanced photocatalytic degradation activity of ZIF-8 doped with Ag_2WO_4 photocatalyst. *J. Taiwan Inst. Chem. Eng.* **2023**, *151*, 105141. [CrossRef]
107. Wu, Y.; Zhu, W.; Yi, G.; Su, X.; Pan, Q.; Oderinde, O.; Xiao, G.; Chen, L.; Zhang, C.; Zhang, Y. Excellent performance of $AgVO_3$@ZIF(Zn, Co) interfacial heterojunction for photodegradation of organic pollutants: Experimental and computational studies. *J. Ind. Eng. Chem.* **2024**, *135*, 377–387. [CrossRef]
108. Wang, L.; Wang, J.; Tang, M.; Wang, C.; Gao, D.; Zhou, Y. Developing a Z-scheme Ag_2CO_3/ZIF-8 heterojunction for the surface decoration of cotton fabric toward repeatable photocatalytic dye degradation. *Appl. Surf. Sci.* **2023**, *610*, 155605. [CrossRef]
109. Liu, J.; Zhan, H.; Wang, P.; Chen, M.; Zhu, X.B.; Han, J.; Fu, B. Assembling BiOBr nanoplates on MIL-125(Ti)–NH_2 via group linkage towards effective dye-contaminated water purification. *J. Solid. State. Chem.* **2024**, *329*, 124408. [CrossRef]
110. Ren, Y.; Li, Y.; Pan, G.; Wang, N.; Xing, Y.; Zhang, Z. Recent progress in CdS-based S-scheme photocatalysts. *J. Mater. Sci. Technol.* **2024**, *171*, 162–184. [CrossRef]